



1 Eddy-Driven effects on solute transport in turbulent channel flows in porous 2 media

3

4

5

6

2, 3, *, Xixian Kang¹, Kun Huang¹, Chong Ma⁶

8

⁹ ¹ School of Environmental Studies, China University of Geosciences, 430074 Wuhan,
¹⁰ China

11 ²School of Geography and Information Engineering, China University of Geosciences,
12 430074 Wuhan, China.

13 ³ Key Laboratory of Mine Ecological Effects and Systematic Restoration, Ministry of
14 Natural Resources, Beijing, 100081.

¹⁵ ⁴The First Geological Brigade of Hubei Geological Bureau, 435000, Huangshi, China.

¹⁶ ⁵ Huaneng Lancang River Hydropower Inc., 650206, Kunming, China.

17 ⁶School of Mathematics and Physics, China University of Geosciences, 430074 Wuhan,
18 China.

19

20 * Corresponding authors:

21 haibo feng@cug.edu.cn



22 **Abstract**

23 Groundwater pollution poses a significant threat to water resource sustainability, yet
24 the role of pore-scale eddies in solute transport remains underexplored. This study
25 investigates the effects of hydrodynamic conditions (flow velocity) and porous media
26 structural parameters (particle size, arrangement) on eddy development and solute
27 transport through laboratory experiments and numerical simulations. A novel three-
28 dimensional (3D) quantitative method for characterizing eddy zones was proposed,
29 revealing the mechanisms of eddy formation and their impact on solute breakthrough
30 curves (BTCs). Results indicate that higher flow velocities and larger particle sizes
31 amplify eddy proportions, leading to pronounced BTC tailing due to delayed solute
32 exchange between main flow stream and eddy zones. The mobile-immobile model
33 (MIM) parameters, particularly the immobile zone ratio ($1-\beta$), showed strong alignment
34 with eddy proportions, reducing inversion ambiguity. Smaller particle sizes diminished
35 early solute breakthrough, while random-packed (RP) media exhibited the slowest
36 solute penetration compared to structured arrangements (SC, FCC, BCC). The study
37 establishes exponential relationships between dilution index and eddy-dominated solute
38 heterogeneity, highlighting structural controls on diffusion coefficients. These findings
39 enhance theoretical frameworks for groundwater solute transport and provide practical
40 insights for optimizing pollution remediation strategies in porous media systems.

41 Keyword: Eddy effect, Porous media, Solute transport, Mobile-immobile model



42 **1 Introduction**

43 Groundwater, as one of the important types of water sources, is characterized by
44 its widespread distribution, abundant reserves, and good water quality, which is often
45 used as a vital water source for industrial and agricultural production ([Danielopol et al., 2003](#);
46 [Foster and Chilton, 2003](#); [Llamas and Martínez-Santos, 2005](#)). However, the
47 intensification of human activities has led to a continuous deterioration of groundwater
48 quality ([Burri et al., 2019](#); [Shah et al., 2003](#)). Approximately 90% of groundwater
49 resources in China are affected by varying degrees of pollution ([Jia et al., 2018](#); [Wang et al., 2018](#)). Once contaminated, remediation is often difficult, resulting in a high
50 vulnerability of most aquifers ([Gorelick and Zheng, 2015](#); [Kalhor et al., 2019](#)). The
51 coordinated development of socio-economic and ecological environments has
52 generated an unprecedented urgent demand for the prevention and control of
53 groundwater pollution. According to the conditions of the groundwater storage
54 media, groundwater can be classified into pore water, fissure water, and karst water
55 ([Kaufmann and Braun, 2000](#)), among which the pore media are widely distributed and
56 easily exploitable, making them the primary water storage medium in aquifers of plain
57 areas ([Gruzałski et al., 2016](#)). However, the vast majority of quantitative studies of
58 groundwater mass and energy migration are based on the "seepage assumption" ([Harr, 2012](#)), which simplifies the complex and curvilinear motion of groundwater within the
59 actual geotechnical void to the linear movement of groundwater through solid particles.
60 This simplification greatly facilitates the construction and solution of models for
61



63 groundwater flow dynamics and solute transport, providing a foundation for the
64 quantitative study of macro-scale groundwater flow and solute fields, which also
65 addressing many practical engineering problems ([Vaughan, 2009](#); [Wang, 2004](#)).
66 However, the actual groundwater flow movement is essentially a complex curved
67 motion ([Hubbert, 1940](#); [Polubarnova-Kochina, 2015](#)). During this process, the intricate
68 boundary morphology can easily form eddies, which has significant effects on the
69 resistance of water flow movement, velocity distribution of flow field, spatial
70 distribution of groundwater solute, and the law of solute migration, especially on the
71 distribution, migration and retention of solute ([Lee and Babadagli, 2021](#); [Li et al., 2023](#);
72 [Zhou et al., 2021](#)).

73 Traditional studies suggest that the migration patterns of pollutants can be
74 described using the advection-diffusion equation, assuming that the dispersion behavior
75 of the solute plume conforms to Fickian laws ([Grindrod and Impey, 1993](#); [Moradi and](#)
76 [Mehdinejadiani, 2018](#); [Zhou and Selim, 2003](#)). [Kreft and Zuber \(1978\)](#) provided an
77 analytical solution for the breakthrough curves (BTCs) indicating that that Fickian BTC
78 is asymmetric in time and symmetrical only in space. However, a large number of
79 studies have found that the BTCs of pollutants migrating through porous media are not
80 symmetrical normal distributions, but rather exhibit significant early arrival and tailing
81 non-Fickian behavior ([Brusseau et al., 1989](#); [de Vries et al., 2017](#); [Rao et al., 1980](#)).
82 This leads to an increased residence time of pollutants in the porous media and
83 significantly slows down the concentration decay process ([Brusseau, 1994](#); [S'imoněk](#)



84 [et al., 2006](#); [Tang et al., 1981](#)). It has been found that eddies have a significant effect on
85 pollutant tailing ([Dou et al., 2019](#); [Zheng et al., 2022](#)). The curvature of pore boundaries
86 and scaling of cross-sectional areas will lead to the water flow to change direction,
87 accelerate, or decelerate, making it prone to the formation of eddies. The complexity of
88 pore structures determines that eddies are one of the most common and easily occurring
89 phenomena in actual groundwater flow, significantly influencing the distribution of
90 flow velocity and the migration of substances. Unfortunately, due to the limitation of
91 the microscopic scale of the porous media, which is usually millimeter or micron level,
92 it is difficult to directly observe the eddy region, resulting in insufficient quantitative
93 identification of eddies. There are few studies considering the influence of eddies on
94 the solute transport process of the porous media from the pore scale, which also makes
95 the mechanism of eddies on the migration of pollutants in porous media seriously
96 ignored for a long time.

97 The currently mobile-immobile model (MIM) is often used to describe the non-
98 Fickian transport behavior observed in solute transport within porous media affected
99 by eddies ([Gouze et al., 2008](#); [Hasan et al., 2019](#); [Karadimitriou et al., 2016](#)). The MIM
100 model divides the water flow into two parts: the mobile zone and the immobile zone.
101 The solute exchange between the different regions occurs through molecular diffusion,
102 and the exchange intensity depends on the concentration difference in different regions
103 ([Gao et al., 2010](#); [Kohne et al., 2004](#)). The parameters related to the MIM model, such
104 as the proportion of the immobile zone, can only be retrieved by fitting the BTCs.



105 Additionally, the uncertainty of the MIM model is increased because the physical
106 meaning of relevant parameters cannot be clearly defined during the calibration process,
107 which limits the range of parameter values.

108 To further explore the generation, development, and evolution of eddies, as well
109 as their influence on solute transport processes under different hydrodynamic
110 conditions (different velocities) and the main controlling factors of porous media
111 structure (different particle sizes and arrangement), this study designed various types
112 of porous media models and conducted a series of laboratorial physical model
113 experiments and numerical simulations. Firstly, a new quantitative characterization
114 method of three-dimensional (3D) eddy area proportion is proposed. Secondly, the
115 mechanism of different flow velocities, particle sizes and arrangement patterns on the
116 formation, development and evolution of eddies and their influence on solute transport
117 was revealed from the 3D pore scale. Finally, the relationship between the parameters
118 of the MIM model and the structural parameters of the porous medium is quantified,
119 which can provide scientific support for the prevention and control of groundwater
120 pollution, and enrich the basic theories of groundwater seepage and solute transport.

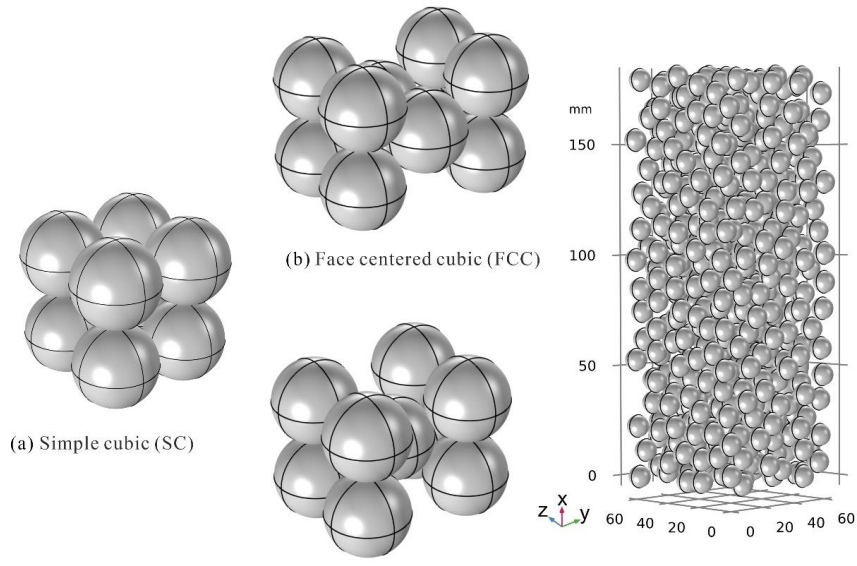
121 **2 Materials and methods**

122 **2.1 Model design and experimental apparatus**

123 To investigate the mechanisms by which the structure of different types of porous
124 media affects the development and evolution of eddies, this study designed four
125 different types of porous media, including simple cubic (SC), face-centered cubic



126 (FCC), body-centered cubic (BCC), and randomly packed (RP). The SC is the loosest
127 pore structure, and the arrangement is gradually tight from FCC to BCC, and the
128 corresponding porosity is 0.476, 0.398, and 0.266, respectively. The randomly packed
129 porosity is 0.645. Subsequently, we can determine the coordinates of each sphere once
130 they achieve mechanical equilibrium. The geometric model of the randomly packed
131 porous media is constructed by integrating MATLAB. It is worth mentioning that the
132 particle sizes of pore media in different arrangement modes are consistent, and a total
133 of 5 mm, 8 mm, 10 mm, 15 mm different particle sizes are designed. The different types
134 of porous media models are shown in Figure 1.

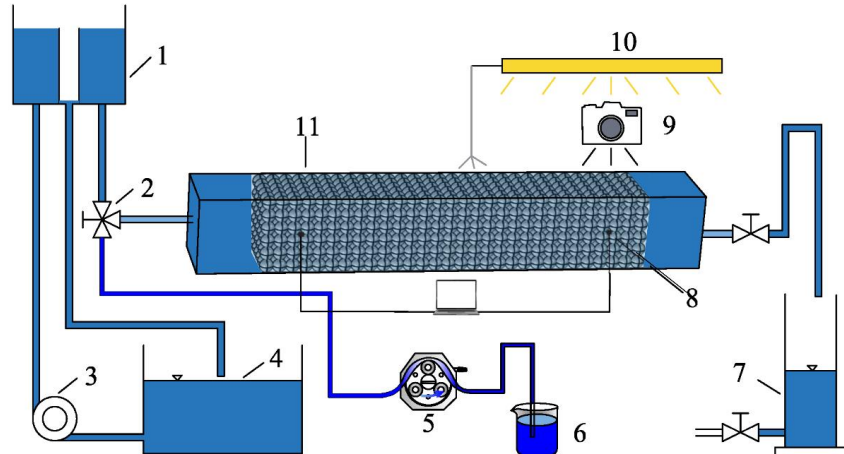


135
136 Figure 1. Diagram of different types of porous media models.

137 Considering the limitations of traditional physical model experiments, we choose
138 the SC packed model to carry out laboratory seepage and solute transport experiments.
139 According to our previous research ([Huang et al., 2013](#)), we found that the wall effect

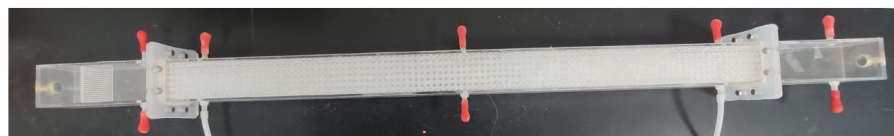


140 (the flow resistance caused by the tube wall) could be disregarded when the number of
141 spheres in the cross-section of the experimental tubes reached 6×6 . The schematic
142 diagram and physical diagram of the experimental device are shown in Figure 2.



1-Fixed head device, 2-Valve, 3-Pump, 4-Water supply tank, 5-Peristaltic pump, 6-brilliant blue,
7-Measurement tank, 8-Pressure sensor, 9-Camera, 10-Illuminant, 11-Experimental section.

(a)



(b)

143
144 Figure 2. Schematic diagram of solute transport experimental setup.

145 The tracer delivery system and imaging system were added on the basis of the
146 seepage experimental device. The experimental tube section is composed of three parts:
147 the inlet and outlet transition section and the porous media section. The total length of
148 the experimental tube section is 150 cm, the pellet filling section is 100 cm, and the
149 length of the inlet and outlet transition section is 25 cm. The transition section is
150 designed to mitigate the effects of inlet and outlet influences. Additionally, a dissipative

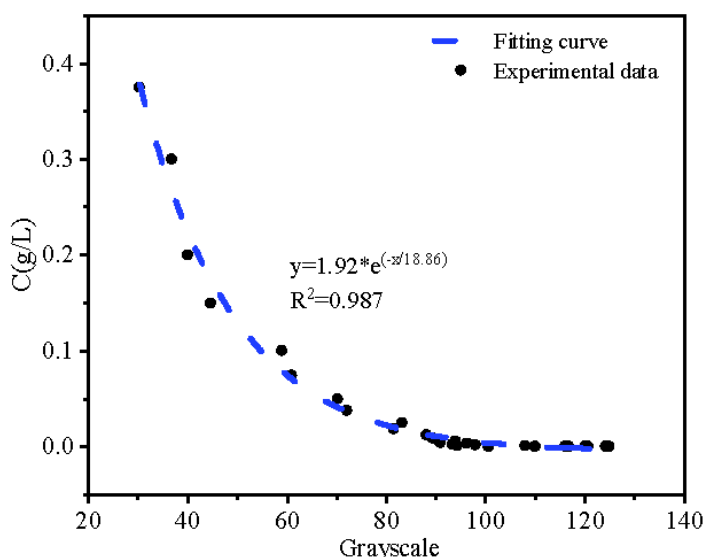


151 plate with numerous small holes is installed at the inlet transition section to ensure a
152 more stable flow of water entering the system. The medium section is filled with
153 artificially bonded cubic spheres arranged in a specific pattern, and pressure
154 measurement ports are located 5 cm away from both the inlet and outlet. The
155 measurement system consists of three components: flow, pressure, and temperature
156 measuring devices. The flow rate after stabilization is calculated using the volumetric
157 method. By monitoring the pressure changes between the two pressure measurement
158 ports using a pressure sensor, a quantitative relationship between seepage resistance
159 and flow velocity can be obtained.

160 To investigate the effects of different influencing factors (such as different flow
161 velocities, particle sizes, and arrangement) on the solute transport process, the selected
162 tracer should not react with the porous media and should have low adsorption properties.
163 Due to its stable chemical properties and good visibility, Brilliant Blue was chosen as
164 the tracer for this solute transport experiment. The photography method involves
165 capturing images or videos of Brilliant Blue concentrations at different time intervals
166 using high-resolution camera (FDR-AX60, SONY). The quantitative relationship
167 between solute concentration and image information can be established by obtaining
168 information from images of a fixed concentration of Brilliant Blue solution (such as
169 grayscale values or RGB values), allowing for the determination of solute
170 concentrations at different times. Compared to the sampling method, the photography
171 method does not disturb the flow field and is easy to operate, which has been widely



172 used. To address the concern regarding light source variation, we implemented a strict
173 protocol: the light source, camera, and column positions were fixed, and each image
174 was corrected using a reference image taken with pure water under identical conditions.
175 Most importantly, the calibration curve was developed under the exact same lighting
176 settings as the experiments, meaning the concentration-grayscale relationship
177 inherently accounts for the specific illumination field, ensuring robust relative
178 measurements. The relationship between the concentration of Brilliant Blue and the
179 grayscale values of the photographs we obtained is shown in Figure 1, displaying a
180 clear negative power-exponential relationship. Strictly speaking, the observation
181 concerning the increased uncertainty in low-concentration estimation from the
182 calibration curve, which is an inherent limitation of the optical method.



183
184 Figure 3. A quantitative relationship between brilliant blue concentration and
185 grayscale image.



186 **2.2 Numerical simulation methods and model validation**

187 It is very difficult or almost impossible to obtain the 3D seepage field of porous
188 media by traditional physical model experiment. With the rapid development of
189 computational fluid dynamics, numerical simulation has been widely used in the study
190 of groundwater seepage ([Banaei et al., 2021](#); [Yang et al., 2019](#); [Yu et al., 2023](#)), which
191 also and has a good effect on the simulation of porous media using COMSOL
192 Multiphysics® ([Banaei et al., 2021](#); [Koohbor et al., 2023](#)). The COMSOL
193 Multiphysics® is a finite element method-based fluid simulation software that can
194 simulate fluid flow in porous media by solving the conservation equations and the
195 Navier-Stokes equations for incompressible fluids. The transport process of solute in
196 porous media was simulated using the advection-diffusion equation coupled with the
197 flow field. And the governing equations are shown as follows:

$$\rho \nabla \cdot \mathbf{u} = 0 \quad (1)$$

$$\rho (\mathbf{u} \cdot \nabla) \mathbf{u} = \mu \nabla^2 \mathbf{u} - \nabla p \quad (2)$$

$$\frac{\partial C}{\partial t} + \nabla \cdot \mathbf{J} + \mathbf{u} \cdot \nabla C = 0 \quad (3)$$

$$\mathbf{J} = -D \nabla C \quad (4)$$

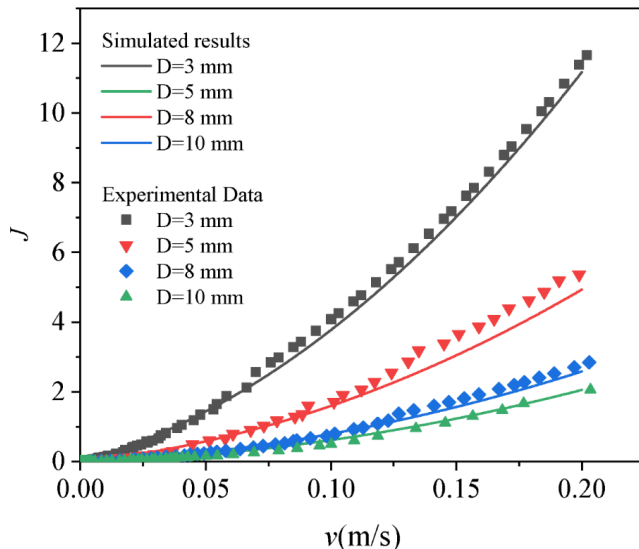
198 where ρ is the fluid density, ∇ is the gradient operator, \mathbf{u} is the velocity vector in 3D
199 coordinate system, μ is the dynamic viscosity, and p is the total pressure. As for the
200 solute field, C is the injection concentration of the solute, \mathbf{J} is the mass flux diffusive
201 flux vector, D is the diffusion coefficient.



202 Experiments and corresponding numerical simulations were conducted on the SC
203 model under different flow velocities. It is essential to ensure that the dimensions of the
204 numerical model are fully consistent with those of the experimental section. The inlet
205 boundary is set as a velocity boundary, the outlet boundary is set as a pressure boundary,
206 and the model wall is set as a no-slip boundary with zero flow. Besides, the density of
207 water is 998.2 kg/m^3 , and the dynamic viscosity is $1 \times 10^{-3} \text{ Pa}\cdot\text{s}$. The concentration at the
208 inlet boundary is set to 0.079 g/L , the right side of the model is set as the outflow
209 boundary, and the wall is set as a zero-flux boundary. The molecular diffusion
210 coefficient of the solute is set to $2 \times 10^{-9} \text{ m}^2/\text{s}$. Then, the corresponding flow field and
211 solute field are obtained by controlling different inlet velocities. The preprocessing of
212 the model has a significant impact on the results of numerical simulations. The overall
213 accuracy of the model mesh generation is controlled by setting the boundary layer and
214 the number of grid elements. On the one hand, the selected mesh size should not be too
215 large, otherwise it will not be able to reflect the real model structure, on the other hand,
216 the mesh size should not be too small, which will consume much more computer
217 resources, and the calculation results cannot even converge. The COMSOL
218 Multiphysics® can offer nine levels of grid sizes, and the mesh sensitivity analysis
219 indicates that the fine-level grid can avoid poor mesh quality and greatly improve
220 computing efficiency. In our previous research, The COMSOL Multiphysics® was also
221 applied to the simulation of the seepage field and solute field in rough conduit media,
222 achieving good results ([Li et al., 2024](#)).



223 To ensure the accuracy of the numerical simulation, we need to validate the
224 simulation results with the experimental data, which are detailed in [Huang et al. \(2013\)](#).
225 We have compared the numerical simulation results with the experimental results, and
226 the relationship between hydraulic gradient (J) and specific discharge (v) in porous
227 media with SC packing is plotted in Figure 4. To avoid confusion, we should point that
228 \mathbf{J} indeed represents the mass diffusive flux vector, which is a vector quantity (bold in
229 italics). Conversely, in Figure 4, J was used to denote the hydraulic gradient, a scalar
230 quantity.



231
232 Figure 4. Comparison of experimental and numerical simulation J - q curves of SC
233 packing porous media.

234 We can see that the hydraulic gradient in the simulation results is slightly less than
235 that in the experimental results; even so, the simulation results fit well with the
236 experimental results overall. When the particle size of spheres remains the same, the
237 hydraulic gradient increases with the increasing specific discharge. While the specific



238 discharge is somewhere the same, a smaller particle size leads to a greater hydraulic
239 gradient. In other words, the smaller particle size needs to overcome the stronger
240 seepage resistance. In this study, the experimental hydraulic data (v - J curves in Figure
241 4) provided the primary validation for the flow field. Since Brilliant Blue is an inert
242 tracer, its transport is predominantly advection-diffusion under the studied conditions.
243 Therefore, accurately replicating the flow field is the most critical factor for reliable
244 solute transport simulations. The strong agreement between experimental and simulated
245 v - J relationships demonstrates the accuracy of the flow field, thereby validating the
246 foundation for the subsequent solute transport results. Therefore, given that the flow
247 field has been rigorously validated and the solute is inert, we are confident that the
248 numerical solute transport results are robust.

249 Besides, we acknowledge that a direct comparison of experimental and numerical
250 concentration fields would be ideal. However, obtaining detailed 3D experimental
251 concentration data within the opaque porous medium is technically challenging with
252 our current setup. Our experimental concentration measurement (via imaging) provides
253 spatially-averaged data at the column outlet (BTCs), but not the internal 3D
254 concentration fields needed for a point-by-point comparison. Therefore, our validation
255 strategy relied on a foundational principle: for an inert solute, the accuracy of the
256 transport simulation is entirely dependent on the accuracy of the flow field. The good
257 agreement in the v - J curve validates the overall flow field. And the solute transport
258 simulation is a direct consequence of the validated flow field and the advection-



259 diffusion equation. It will clarify that for an inert tracer, no additional solute-specific
260 calibration is performed or required, as the transport parameters are known.

261 **3 Results and discussion**

262 **3.1 Identification of eddy zone in 3D scale**

263 Due to the complexity of porous media structure, the streamlines are obstructed
264 during the seepage process, resulting in the formation of numerous eddy zones.
265 However, it is very difficult to directly extract the volume of eddy area in 3D porous
266 media. Different methods for identifying the eddy area in 3D scale was proposed based
267 on the definition of zero flux in eddy zones ([Zhou et al., 2019](#)) and the velocity
268 probability density function (PDF), see details in [Bijeljic et al. \(2013\)](#).

269 Taking the SC model as an example, firstly, we sliced the 3D porous media model
270 using the XZ plane (with the X-axis as the flow direction). Multiple cross-sections are
271 set along the Y-axis to ensure that the number of slices can effectively cover the entire
272 model, as shown in Figure 5(a), and further export the velocity field data of different
273 2D sections. We can see that the colors at different positions are different, reflecting
274 different flow velocities through the local magnification of the 2D slice flow field, as
275 shown in Figure 5(b). The flow velocity is lower in the areas where eddies are generated,
276 while the flow velocity at the main flow stream is relatively large. To analyze the flow
277 velocity characteristics of the eddy area and their impact on solute transport, we further
278 obtained the flow velocity and concentration data at different times along the white
279 section line (which includes the main flow stream and the eddy area, see Figure 5(b))



280 according to the numerical simulation results, as shown in Figure 5(c). It can be seen
281 from Figure 5(c) that the flow velocity curve exhibits three peak velocity segments and
282 two low velocity segments. Combined with Figure 5(b), we can see that the region with
283 high velocity corresponds to the main flow stream, while the region with low velocity
284 corresponds to the eddy area. The flow velocity of the main flow stream is significantly
285 higher than that of the eddy area, approximately 20 times the velocity in the eddy area.
286 Moreover, we can clearly observe that there is a significant point of mutation in the
287 flow velocity between the main flow stream and the eddy zone (the blue curve in Figure
288 5(c)). In addition, we selected two arbitrary moments (t_1 , t_2) during the solute
289 attenuation process to obtain the solute concentrations in both the main flow stream and
290 the eddy zone. It can be observed that the solute concentrations in the eddy zone are
291 significantly higher than those in the main flow stream. This is due to the relatively low
292 flow velocity in the eddy zone, along with the bending and deflection of streamlines,
293 which allows the solute to be captured by eddies, slowing down the diffusion process
294 into the main flow stream.

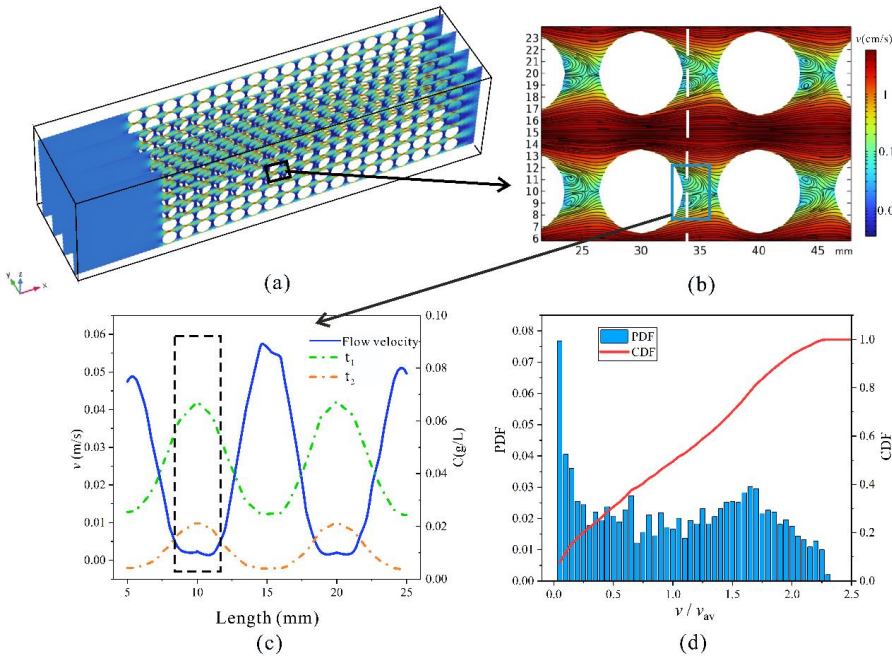
295 To compare the velocity differences at various positions within the flow field, we
296 performed normalization using the average flow velocity (v_{av}), which is actually the
297 inlet flow velocity. We classify the velocities at different positions in 3D space and
298 obtained the velocity probability density function (PDF) and cumulative probability
299 density function (CDF) under different inlet flow velocities, allowing us to compare the
300 changes in the proportion of low-velocity areas under different flow velocity conditions.



301 Based on the velocity difference between the main flow stream and the eddy zone, we
302 can obtain the critical flow velocity (v_c), which is the significant point of mutation
303 mentioned above. The process of using the PDF and CDF to quantify the eddy area in
304 a 2D slice, which is then integrated to obtain the 3D proportion, is indeed a key aspect
305 of our analysis, which divided into five steps: Firstly, using the self-developed
306 MATLAB code to process the acquired 2D seepage field data. For a given 2D slice (e.g.,
307 an XZ plane at a specific Y-coordinate, as in Figure 5a), we export the velocity
308 magnitude at every grid point within the fluid domain. We then calculate the PDF and
309 CDF of these velocity values for that specific slice. The horizontal axis of this plot is
310 the velocity normalized by the average inlet velocity (v/v_{av}). As shown in Figure 5(c),
311 we identify a critical flow velocity (v_c) that represents the inflection point separating
312 the low velocities in the eddy zones from the high velocities in the main flow channels.
313 The value of the CDF corresponding to this normalized critical velocity (v_c/v_{av}) directly
314 gives the area fraction of that specific 2D slice where the velocity is less than or equal
315 to v_c . This area fraction is our quantitative measure of the "eddy area" for that slice. By
316 repeating this PDF/CDF analysis for a dense series of parallel 2D slices spanning the
317 entire model (along the Y-axis), we obtain the eddy area fraction for each slice. The
318 eddy area proportion for the entire 3D model is then calculated by integrating
319 (averaging) these 2D area fractions across all slices. This method provides a robust and



320 objective way to quantify the complex 3D eddy volume from 2D slice data.



321

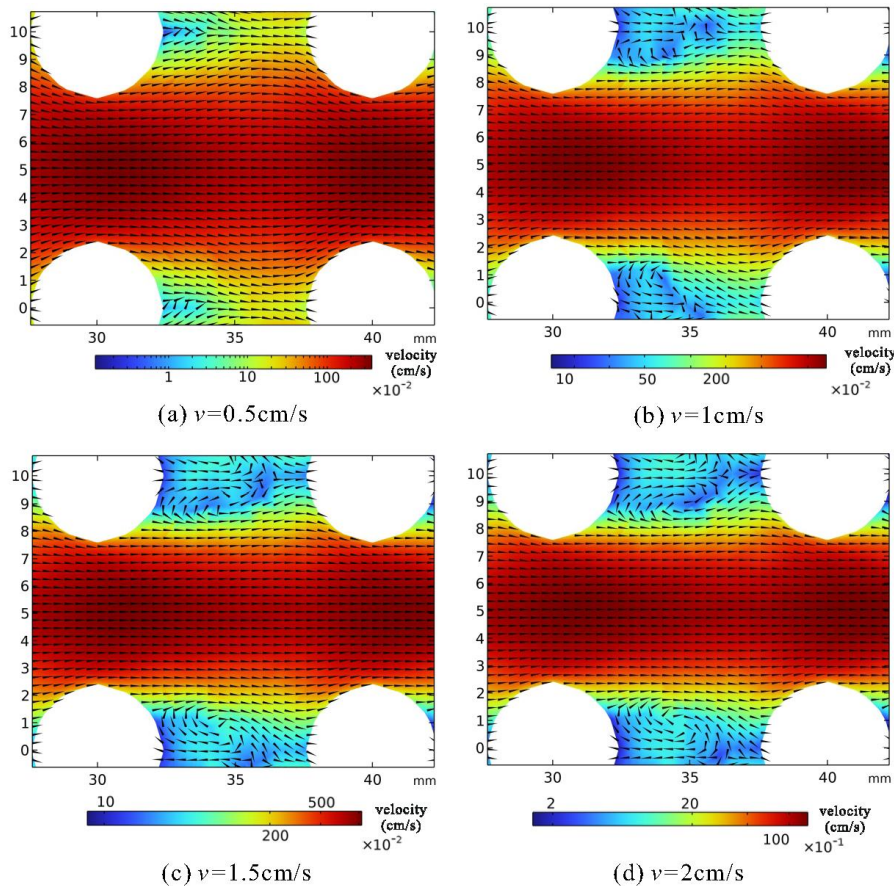
322 Figure 5. Schematic diagram of eddy extraction in porous media.

323 3.2 Effects of different flow velocities on solute transport

324 We selected the SC model with particle size of 10 mm to conduct numerical
325 simulations at four different flow velocities (including 0.5 cm/s, 1 cm/s, 1.5 cm/s, and
326 2 cm/s), and the 2D slice flow fields are shown in Figure 6. The Reynolds numbers
327 corresponding to different flow velocities range from a minimum of 113 to a maximum
328 of 1697, which can provide a standardized metric to characterize the flow and will be
329 accompanied by a discussion clarifying that the observed eddy formation is a result of
330 inertial effects within the laminar flow regime, rather than full turbulence. We have
331 chosen to maintain our analysis based on direct flow velocity for the specific objectives
332 of this study. Our focus is on establishing a direct, intuitive link between the



333 hydrodynamic driving force (velocity) and the resulting eddy development and solute
334 transport behavior. The red areas indicate the main flow stream with high velocity,
335 while the blue areas represent the low-velocity regions formed in the porous medium
336 structure.



337
338 Figure 6. The 2D slice flow fields of the SC model with a particle size of 10 mm at
339 different flow velocities.

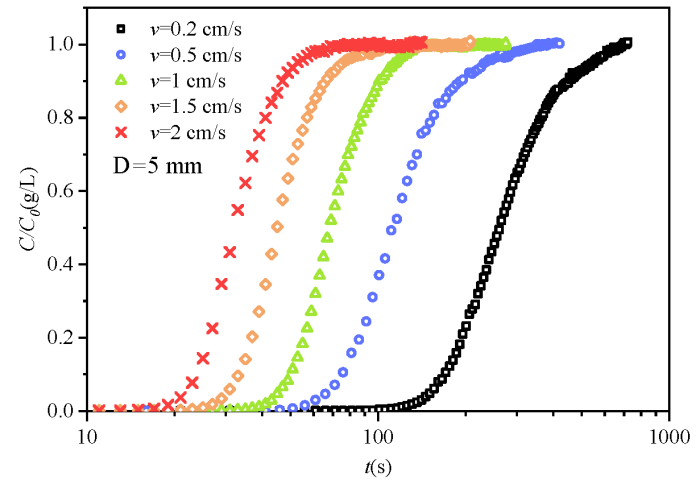
340 We can see from Figure 6 that the flow velocity in the main flow stream is
341 significantly greater than that in the eddy area. When the flow velocity is 0.5 cm/s, the



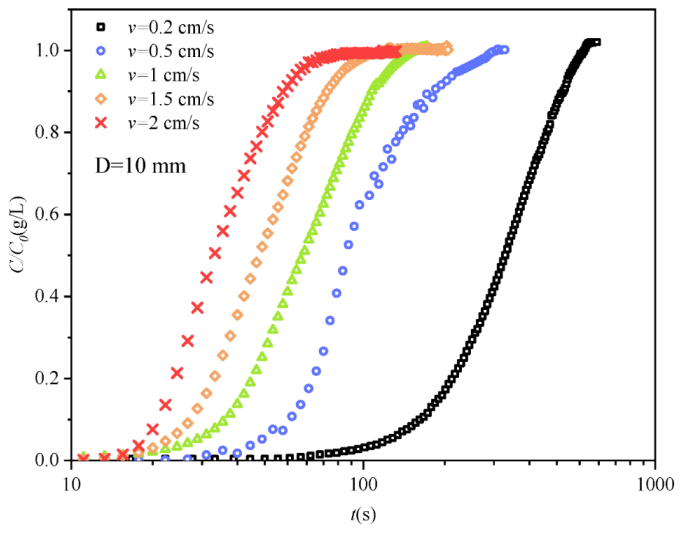
342 streamlines are deflected due to obstructions, leading to the formation of eddies;
343 however, the eddy area proportion is quite small. With the continuous increase of flow
344 velocity, we can obviously see that the eddy proportion increases significantly. This
345 aligns with our previous research conclusions that the eddy proportion will ultimately
346 approach a theoretical maximum value ([Xiong et al., 2024](#)). When the flow state
347 developed to a fully stable condition, we continuously injected the brilliant blue and
348 conducted solute transport experiments in SC model porous media with particle sizes
349 of 5 mm and 10 mm, using five flow velocities of 0.2 cm/s, 0.5 cm/s, 1 cm/s, 1.5 cm/s,
350 and 2 cm/s. The BTCs under different flow velocities are obtained, as shown in Figure
351 7, where the horizontal coordinate was logarithmic and the vertical coordinate
352 normalized the concentration (C/C_0). And the corresponding dilution concentration
353 under different inlet flow velocities is defined as the respective initial concentration
354 (C_0).



355



356



357

Figure 7. The BTCs of SC model porous media with 5 mm and 10 mm particle sizes

358

at different flow velocities.

359

We can see from Figure 7 that the BTCs for both particle sizes shift to the left as

360

the flow velocity increases, indicating that the penetration time decreases. The

361

residence time of water within the pore space increases at lower flow velocities. This

362

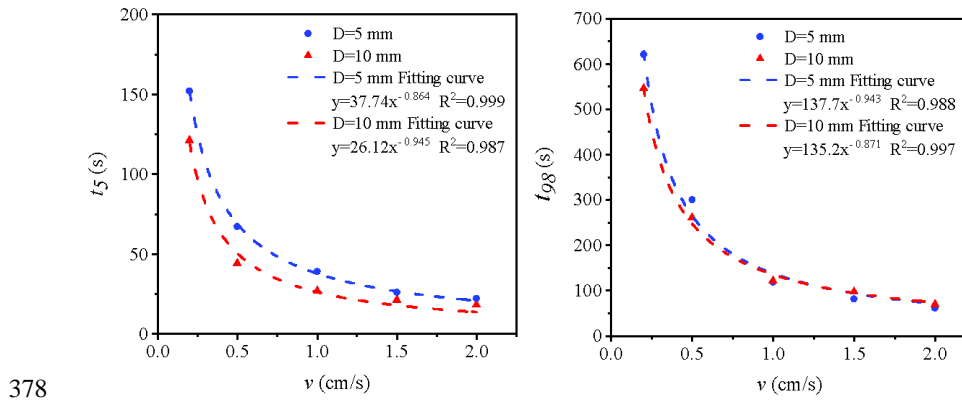
longer contact time allows for a more complete solute equilibration via diffusion

363

between the main flow and the larger, more developed eddy zones present at lower



364 velocities. Consequently, a greater mass of solute is stored in the eddies, which is then
365 released slowly, causing the pronounced tailing. At higher velocities, the reduced
366 contact time and different eddy dynamics limit this equilibration process, leading to less
367 tailing. This correction accurately reflects the interplay between advection timescales
368 and diffusive exchange. Although the tailing of the BTCs is a consistent and robust
369 physical observation, the definitive quantitative analysis of concentrations at very low
370 values ($C/C_0 < 0.05$) is constrained by the increasing uncertainty of the optical
371 calibration method at these levels. Therefore, the specific values in the late-time tail
372 should be interpreted with appropriate consideration of this methodological limitation.
373 To further quantify the eddy effect at different flow velocities and their impact on the
374 characteristics of the BTCs, we established a quantitative relationship between the
375 times corresponding to the BTC concentrations reaching 5% and 98% of the input
376 solute concentration (t_5 and t_{98}) (Hou et al., 2018) and the different flow velocities,
377 respectively, as shown in Figure 8.



378



379 Figure 8. The relationship between characteristic times (t_5 and t_{98}) of BTCs and

380 different velocities with different particle sizes.

381 It can be seen from Figure 8 that t_5 and t_{98} show a power-law decreasing
382 relationship with the flow velocity, indicating that eddy effect has a significant
383 influence on the penetration process of solute. With the flow velocity increases, the
384 eddy area proportion continues to increase, while the proportion of the main flow
385 stream decreases. The increase in flow velocity within the main flow stream results in
386 the solute arriving earlier. Additionally, it can be observed that the reduction of t_{98} is
387 significantly greater than that of t_5 . Taking the porous medium with a particle size of 5
388 mm as an example, when the flow velocity increases from 0.2 cm/s to 2 cm/s, the value
389 of t_5 decreases by approximately 130 s, while the value of t_{98} decreases by about 450 s,
390 indicating that the changes of flow velocity have a more pronounced effect on the tailing
391 process of the BTCs.

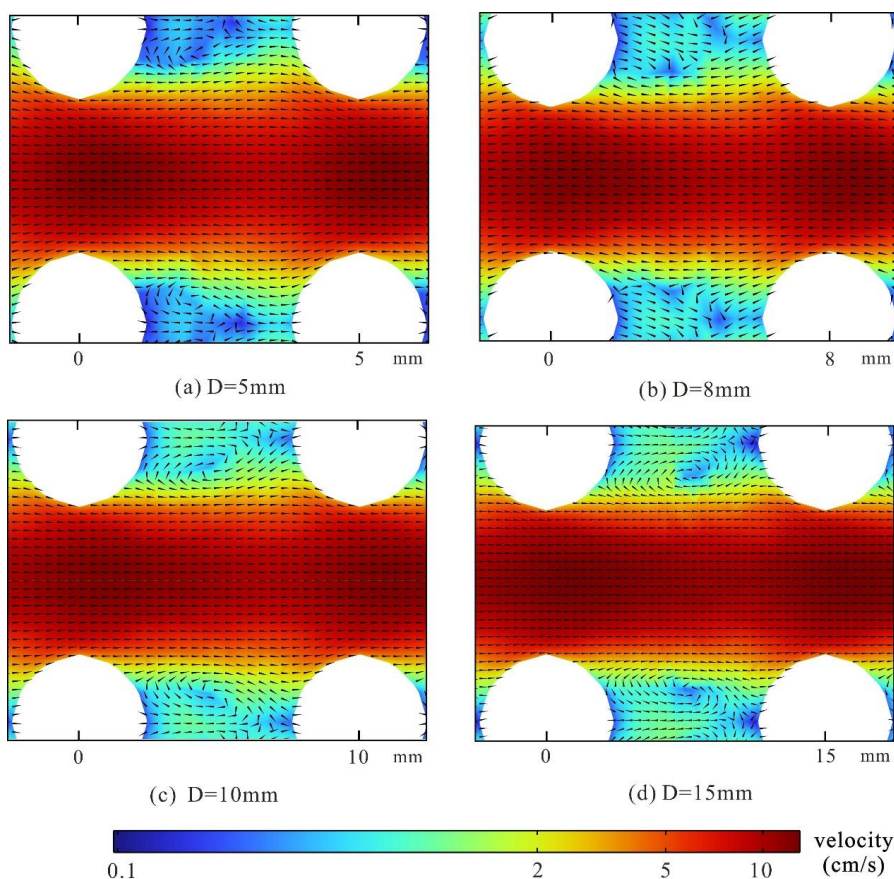
392 **3.3 Effects of different particle sizes on solute transport**

393 The SC model porous media consisting of four different particle sizes (including
394 5 mm, 8 mm, 10 mm, 15 mm) was selected for related numerical simulations. The inlet
395 flow velocity is controlled at a constant 2 cm/s, and the 2D slice flow field is shown in
396 Figure 9. In this study, for a given packing arrangement (e.g., Simple Cubic - SC), the
397 porosity remains constant regardless of the particle size. This is a fundamental
398 characteristic of regular, ordered packings; the porosity is determined solely by the
399 geometric arrangement of the spheres. Therefore, when we investigate the effect of



400 particle size (e.g., 5 mm, 8 mm, 10 mm, 15 mm spheres in an SC packing), we are
401 specifically isolating the effect of scaling the pore geometry (i.e., the absolute size of
402 the pores and throats) while the porosity, a measure of the pore volume fraction, is held
403 constant. This allows us to independently analyze the impact of the particle size on eddy
404 development and solute transport.

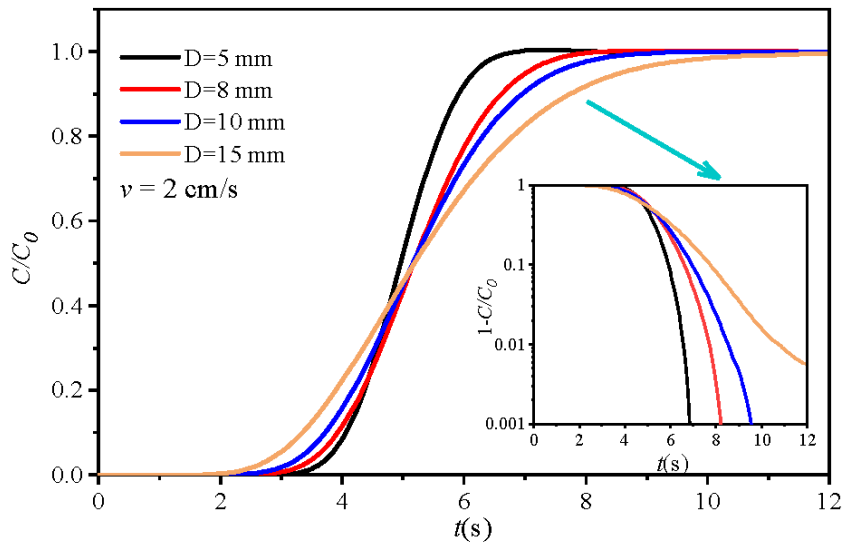
405



406
407 Figure 9. Schematic diagram of the flow field of SC model porous media with
408 different particle sizes ($v=2\text{ cm/s}$).



409 To facilitate the comparison of flow fields between different particle sizes, we
410 adjusted the scale to ensure that the different particle sizes appear consistent. Then, it
411 is easier to visually compare the velocity differences between the low-speed eddy area
412 and the high-speed main flow stream. In Figure 9, the blue area represents the low-
413 velocity eddy area, while the red area indicates the high-velocity main flow stream.
414 Besides, we can observe that when the flow velocity remains constant, the larger
415 particle size led to the larger eddy area and larger rotational velocity inside the eddy
416 area. To explore the impact of different eddy developments on solute transport, we
417 obtained the BTCs under various particle size conditions after injecting the solute, as
418 shown in Figure 10.

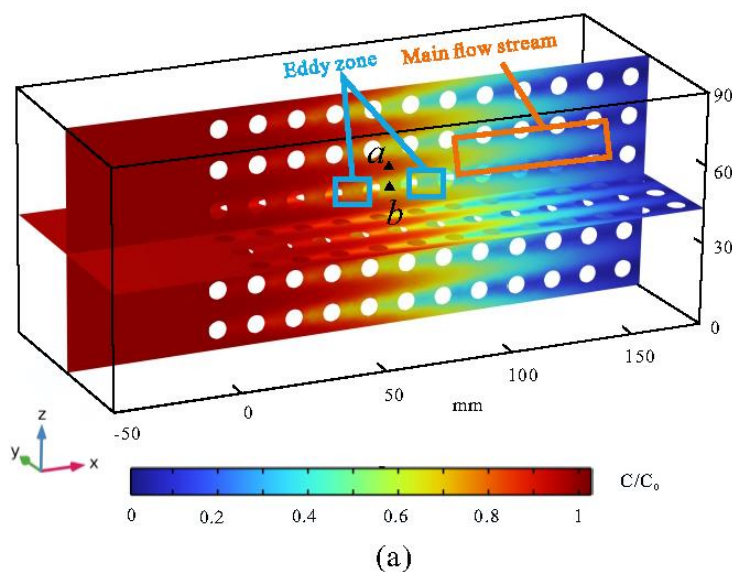


419
420 Figure 10. The BTCs of SC model porous media with different particle sizes.

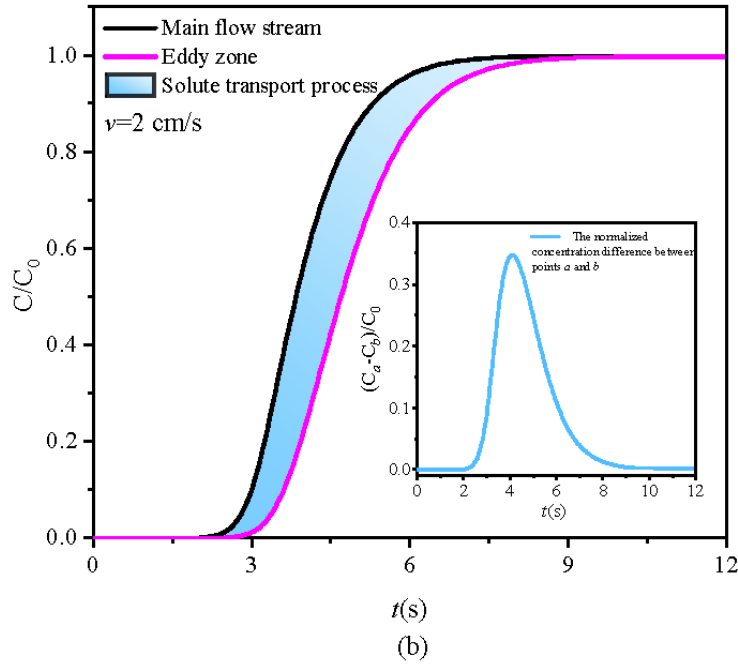
421 We found that the BTCs of different particle sizes show significant differences,
422 exhibiting anomalous early arrival times under the same flow velocity conditions. The



423 BTCs of the porous media with a particle size of 15 mm shows the earliest breakthrough,
424 while the solute penetration the porous medium with a particle diameter of 5 mm the
425 slowest. Furthermore, as the particle size decreases, there is a diminishing trend in the
426 early breakthrough phenomenon of the solute, which is consistent with the above results
427 of flow fields with different particle sizes (eddy development). In the process of solute
428 transport in porous media, the rapid flow in the main flow stream significantly
429 influences the early arrival of the BTCs. To more intuitively observe the morphology
430 of solute peak, we selected a porous media model with a particle size of 15 mm as an
431 example and obtained the solute distribution at 5 seconds after solute injection, as
432 shown in Figure 11(a). In addition, we selected two characteristic points (points *a* and
433 *b* in Figure 11(a)) in the main flow stream and the eddy area, respectively, and obtained
434 their BTCs, as shown in Figure 11(b).



435



436

437 Figure 11. (a) The solute field distribution of SC model porous media ($t = 5$ s, $D = 15$
438 mm, D is particle size). (b) The comparison of the BTCs between the main flow
439 stream and the eddy area.

440 We can see that due to the rapid flow in the main flow channels, multiple distinct
441 solute peak leading edges have been observed. The concentration of solute in the eddy
442 area is significantly lower than that in the main flow stream, and the concentration of
443 solute in the eddy area shows an obvious lag compared with that in the main flow stream.
444 We selected the feature points a and b of the main flow stream and eddy area
445 respectively, and obtained their normalized concentration curves over time, as shown
446 in Figure 11 (b). It can be observed that due to the lag in the eddy area, the solute
447 concentration in the main flow stream is always greater than that in the eddy area. The



448 shaded blue area in Figure 11(b) represents the process of solute transfer between the
449 main flow stream and the eddy area caused by the concentration difference between the
450 two points. We further magnified this process and plotted the normalized concentration
451 difference between the main flow stream and the eddy area (the feature points *a* and *b*).
452 The concentration peaked at 4.1 seconds, showing a trend of initially increasing and
453 then decreasing, and exhibiting a trailing asymmetry, which indicating that the mass
454 transfer rate between the main flow stream and the eddy area slows down.

455 To quantify the impact of eddy effect on the degree of heterogeneous distribution
456 of solute under different particle size conditions, the dilution index proposed by
457 [Kitanidis \(1994\)](#) was used to characterize the dilution state of solute plumes during
458 solute transport. The value of the dilution index represents the volume of the solute
459 plume within the pore volume of the porous media. For continuous injection scenarios,
460 the value of the dilution index closer to 1 indicates a higher ratio of the solute plume
461 occupying the entire pore volume of the media. Once the solute is injected into the
462 porous media, due to the inhomogeneity of the medium structure and flow field, the
463 value of the normalized dilution index will gradually increase. Then, the normalized
464 dilution index can reflect the inhomogeneity of the solute distribution in the porous
465 media. Besides, [Dou et al. \(2018\)](#) evaluated the impact of eddy effect on the uneven
466 distribution of solutes in fractured media using the dilution index. The equation for the
467 solute dilution index $E(t)$ in 3D porous media is as follows:

$$E(t) = \exp \left[- \int_V p(x, y, z, t) \ln(p(x, y, z, t)) dV \right] \quad (5)$$

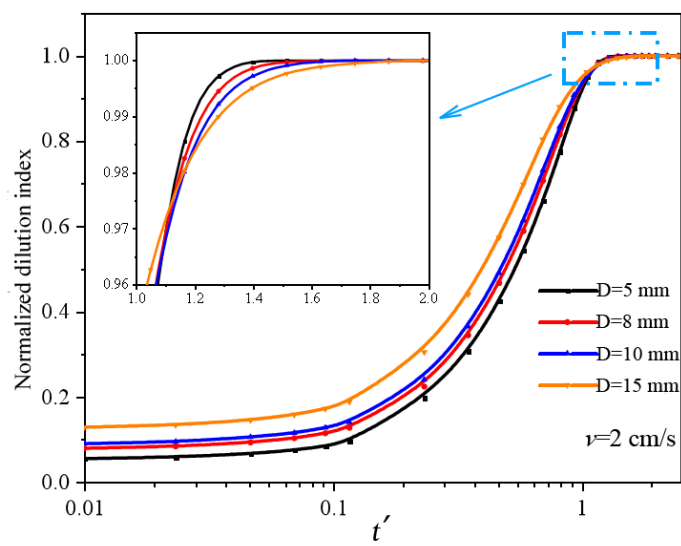


$$p(x, y, z, t) = \frac{c(x, y, z, t)}{\int_V c(x, y, z, t) dV} \quad (6)$$

468 where $p(x, y, z, t)$ is the distribution function of the mass. In this study, the normalized
469 dilution index was used to quantify the influence of eddy effect on the uneven
470 distribution of solute in porous media with different particle sizes. When the flow
471 velocity is 2 cm/s, the relationship between the normalized dilution index of porous
472 media and the dimensionless time parameter t' (the pore volume) with different particle
473 sizes was shown in Figure 12. The t' represents the time process of solute transport, and
474 the equation is as followed:

$$t' = \frac{Qt}{Al} \quad (7)$$

475 where Q is the flow flux at the outlet, t is the time of solute transport, and Al is the
476 volume of the pore.



477



478 Figure 12. The relationship between the normalized dilution index and the
 479 dimensionless time parameter (SC models).

We can see from Figure 12 that the normalized dilution index varies with the dimensionless time parameter in three stages: Firstly, when $t' < 0.12$, the normalized dilution index increases slowly; when $0.12 < t' < 1$, the normalized dilution index increases sharply; and while $t' > 1$, the normalized dilution index remains almost stable, respectively. In the initial stage of solute entering the porous media, the solute preferentially transfers in the main flow stream, while the transfer to the eddy area is still relatively low. Then, the solute transport between the main channel and the eddy area gradually increases. In the later stage of solute transport, the retention of the solute by the eddy area results in a pronounced tailing effect during the penetration process. In addition, we found that larger particle sizes lead to larger normalized dilution index when $t' < 1$, which is related to the pore structure formed by the SC models with different particle sizes and the development of the eddies. For porous media with larger particle size, the larger volume of a single pore leads to a larger volume of eddy area, resulting in a higher degree of inhomogeneity of the solute distribution. When $t' > 1$, a completely opposite trend is observed.

495 As we know, larger particle sizes lead to a higher eddy proportion and greater
496 initial flow heterogeneity. However, the larger individual pore bodies in these media
497 also host larger, more coherent eddy structures. While these large eddies initially trap
498 solute and create a highly uneven distribution (low normalized dilution index for $t' \leq 1$),



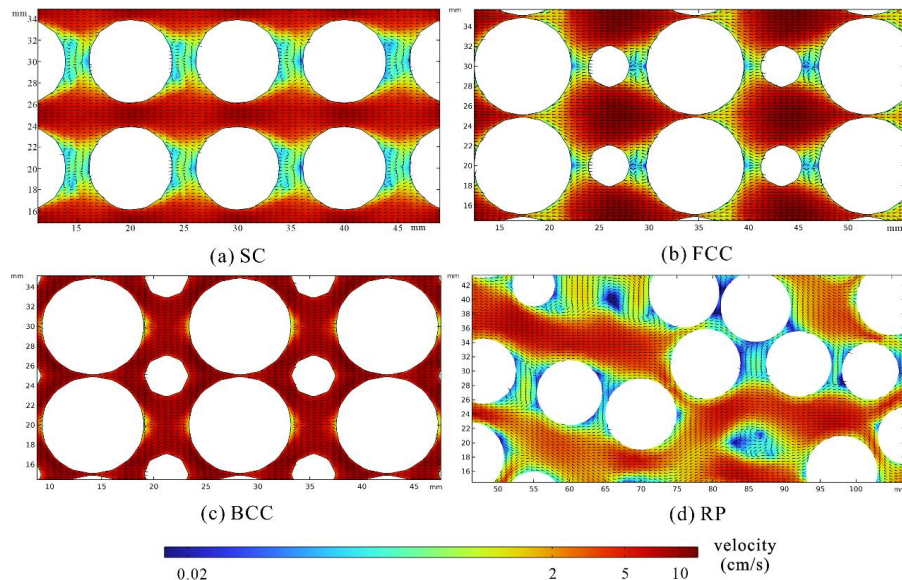
499 they also provide a larger volume for diffusive mixing to act upon over time. The mass
500 transfer between the main channel and these sizable eddy zones is governed by
501 diffusion across longer characteristic paths, making it a slower process. Consequently,
502 the system with larger grains requires a longer time to achieve a homogeneous state.
503 After the primary advective pulse has passed ($t' > 1$), this slower, more complete back-
504 diffusion from the large, well-developed eddies eventually leads to a higher degree of
505 homogeneity (a higher normalized dilution index) compared to systems with smaller
506 grains, where the pore structure is more confined and complex, potentially limiting the
507 final extent of mixing. This interpretation, consistent with the mechanisms discussed in
508 studies like [Dou et al. \(2018\)](#), highlights the time-dependent competition between
509 heterogeneity-driven trapping and volume-enhanced diffusive mixing.

510 In this study, we employed the dimensional dimensionless time parameter t' (e.g.,
511 Figure 12) strategically. Using actual time as the x-axis in several figures (e.g., Figures
512 7 and 10) was intentional, as it allows for a more intuitive understanding of the temporal
513 scale of the observed non-Fickian transport phenomena, such as the absolute time of
514 early arrival and the duration of tailing. This provides a direct, physical sense of the
515 retardation caused by eddies. Meanwhile, the use of dimensionless time in other figures
516 facilitates the comparison of the shape of the BTCs independent of the system's specific
517 volume. We believe this dual approach offers complementary insights.

518 **3.4 Effects of different arrangement patterns on solute transport**



519 Different arrangement modes have significant influence on the structure of porous
520 media. This section will describe in detail the eddy evolution of porous media with
521 different arrangement modes (including SC, FCC, BCC and RP), when the inlet flow
522 velocity is 2 cm/s, the obtained flow field is shown in Figure 13.



523 Figure 13. Schematic diagram of flow field and eddy area of porous media with
524 different arrangement modes ($v = 2$ cm/s).

526 We can see from Figure 13 that the flow fields of porous media with different
527 arrangement modes are completely different, and different colors respectively represent
528 the main flow stream with high flow velocity (red area) and the eddy area with low
529 flow velocity (blue area). Due to the relatively regular structure of the porous medium
530 in SC model, the pore abdomen can provide a larger development space for eddies, so
531 the volume of the eddy area formed by the SC model is larger than that of the other
532 three arrangements. The spatial positions of eddies in porous media with different



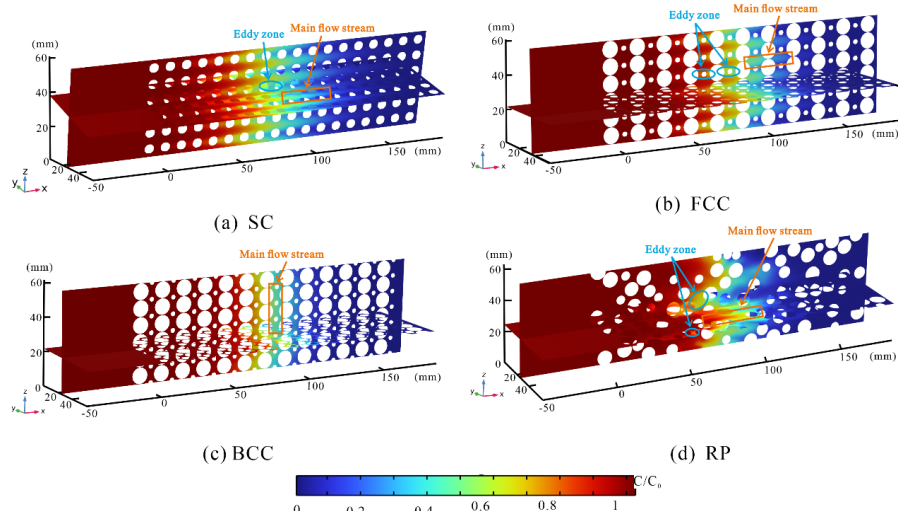
533 arrangement modes are also completely different. As for the RP model, we have
534 observed several very interesting phenomena: The structure is further complicated due
535 to the randomness of the arrangement of the spheres. On the one hand, two distinct
536 preferential flow channels are formed; on the other hand, we observed regions with
537 lower flow velocities, called dead-end-pores ([Bordoloi et al., 2022](#)). The identified eddy
538 zones are not stagnant regions but are characterized by active recirculation. As
539 evidenced by the velocity profile in Figure 5(c), the flow velocity within these zones,
540 while significantly lower than in the main flow channels, is distinctly non-zero. This
541 observation is consistent with the findings of [Bordoloi et al. \(2022\)](#), who emphasized
542 that laminar vortices enhance dispersion through their inherent rotational motion. The
543 quantification of these dynamic eddy zones forms the basis for analyzing their role in
544 solute mass transfer and the emergence of non-Fickian transport behavior.

545 Besides, we also agree that porosity is a fundamental property that profoundly
546 influences flow and transport. We recognize that porosity is not an independent variable
547 here but is a direct consequence of the packing geometry. The substantial difference in
548 porosity (e.g., almost 2x between SC and BCC) is an inherent and defining
549 characteristic of these distinct arrangements. Therefore, the analysis in Section 3.4
550 inherently addresses the combined effect of the specific pore structure and the resulting
551 porosity. Discussing porosity as a separate, parallel factor to arrangement would create
552 a mismatch in the logical hierarchy of influencing factors, as porosity is an emergent
553 property of the arrangement. Our approach was to treat "arrangement" as a holistic



554 factor that encapsulates both the geometric configuration and the resultant porosity. We
555 believe this provides a more integrated understanding of how systematic changes in the
556 medium's architecture control eddy development and solute transport.

557 To understand the influence of different arrangement patterns forming eddies on
558 solute transport, we obtained the solute distribution characteristics in various porous
559 media at 3 s after injection, as shown in Figure 14.

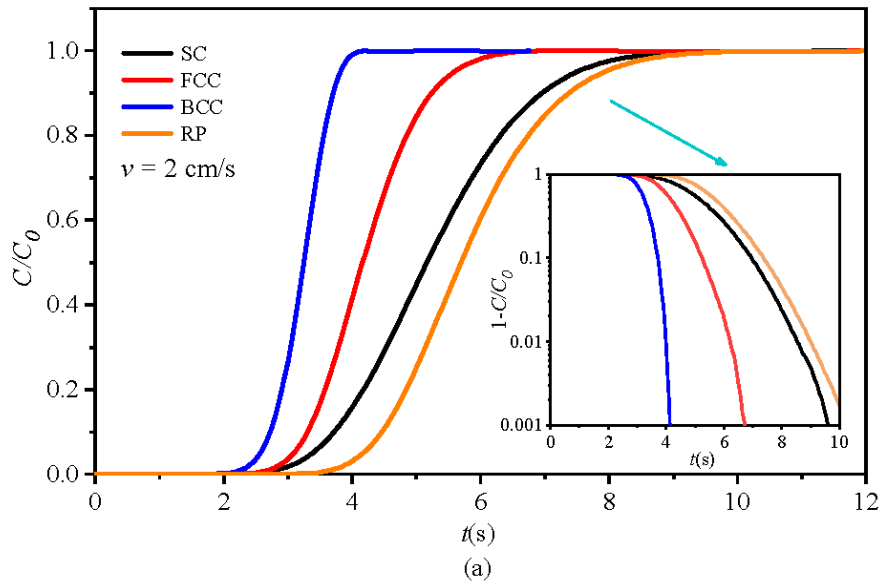


560
561 Figure 14. Solute distribution in porous media with different arrangement patterns.

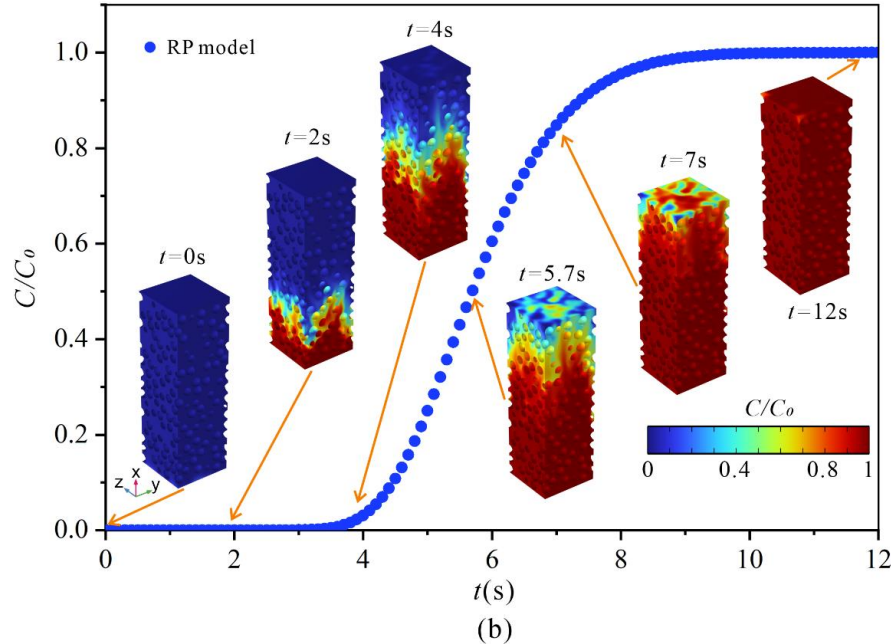
562 We can see from Figure 14 that different types of porous media models all present
563 relatively obvious preferential flow channels, although they differ from each other. The
564 Figure 14(a) show that the preferential flow channel formed are parallel to each other
565 due to the good connectivity of the pore abdomen in the SC model. The Figure 14(b)
566 and (c) indicate that the difference in solute distribution between the FCC and BCC
567 porous media is primarily manifested in the eddies caused by different pore structures.
568 Compared to the FCC model, an additional sphere present in the pore abdomen of the



569 BCC model occupy more pore space, resulting in a lower eddy proportion, which causes
570 the solute peak in the BCC model to appear more uniform. The Figure 14(d) shows that
571 the RP porous media structure is more chaotic, leading to a more uneven solute front
572 with multiple preferential flow paths. Additionally, we further obtained the BTCs of
573 porous media with different arrangements at a flow velocity of 2 cm/s, especially
574 detailing the solute penetration process at different times in the RP model of porous
575 media, as shown in Figure 15.



576



577

(b)

578 Figure 15. (a) The BTCs of different types of porous media with flow velocity of 2
 579 cm/s. (b) The RP model penetration process at different times ($v=2$ cm/s).

580 We can see from Figure 15(a) that the characteristics of the BTCs of porous media
 581 models with different arrangements are completely different when the flow velocity
 582 remains consistent. The penetration process of the BCC model is the fastest, followed
 583 by the FCC and SC models, while the penetration process of the RP model is the slowest.
 584 Among different types of porous media models, the RP model has the highest porosity,
 585 followed by the FCC model, while the BCC model has the lowest porosity, which
 586 indicate that the structure has a significant impact on the solute penetration process. To
 587 compare the effect of eddies on the tail of the BTC, the $1-C/C_0$ logarithmic coordinate
 588 plot is used to process the BTCs (see Figure 15(a)). We noticed that the BTCs of the SC
 589 model and the RP model are nearly overlapping at the tail, and the higher eddy area



590 proportion lead to the greater impact on the trailing effect. It is worth noting that the
591 numerical results, including the low-concentration tails down to relative concentrations
592 of 0.001, are not significantly affected by numerical dispersion. The observed tailing in
593 the BTCs (e.g., Figure 15a) is a physical phenomenon resulting from mass exchange
594 between the mobile zone and the eddy (immobile) zones, not a numerical artifact,
595 thereby confirming the reliability of our conclusions regarding tailing behavior.

596 Specifically, the first arrival time (t_5) and the late-stage tailing time (t_{98}) are
597 extracted from the BTCs for each arrangement (SC, FCC, BCC, RP). These metrics
598 provide a direct quantitative measure of the "early arrival" and "tailing" phenomena,
599 respectively. The eddy zone proportion and characteristic breakthrough times for
600 different packing arrangements at an average inlet velocity of 2 cm/s are shown in Table
601 1.

602 Table 1. The eddy zone proportion and characteristic breakthrough times for different
603 packing arrangements at an average inlet velocity of 2 cm/s.

Arrangement	Eddy Zone Proportion	t_5 (s)	t_{98} (s)
SC	0.148	3.35	8.10
FCC	0.061	3.05	5.95
BCC	0.008	2.60	3.95
RP	0.040	4.15	8.55

604 Table 1 has been added summarizing the eddy zone proportion alongside the
605 corresponding t_5 and t_{98} values for each packing structure. This quantitative data reveals
606 a clear and consistent trend. The eddy zone proportion, which is a direct consequence
607 of the pore structure created by the packing arrangement, shows a strong correlation



608 with the characteristic times. The quantitative relationship between packing
609 arrangement, eddy development, and solute transport characteristics is unequivocally
610 demonstrated in Table 1. The results indicate that the pore structure, determined by the
611 specific packing arrangement, exerts a primary control on the proportion of eddy zones.
612 This proportion, in turn, directly governs the key features of non-Fickian transport. A
613 clear positive correlation is observed between the eddy zone proportion and the late-
614 time tailing, quantified by t_{98} . For instance, the SC arrangement, with the highest eddy
615 proportion (0.148), exhibits the most pronounced tailing ($t_{98} = 8.10$ s), whereas the BCC
616 structure, with a minimal eddy proportion (0.008), shows the fastest clearance ($t_{98} = 3.95$
617 s). While the early arrival time (t_5) is generally earlier in structures with fewer flow
618 obstructions (e.g., BCC), the significantly delayed arrival in the RP model underscores
619 the additional influence of flow path tortuosity and connectivity, beyond the mere
620 volume of eddy zones.

621 This quantitative analysis powerfully substantiates our qualitative arguments. It
622 demonstrates unequivocally that the packing arrangement controls solute transport by
623 determining the development of eddies, which in turn quantifiably governs the degree
624 of both early arrival and tailing observed in the BTCs. This provides a robust, data-
625 driven link between medium structure and non-Fickian transport dynamics.

626 **4 Solute transport model**

627 The solute transport model is of significant importance for predicting and
628 quantifying the process of solute migration. The conventional mobile-immobile (MIM)



629 transport model is used to describe the non-Fickian transport behavior such as early
630 arrival and trailing in porous media. Considering the complexity of the porous media
631 structure, the MIM model divides the pores into mobile and immobile regions. The
632 solute mass exchange occurs between the mobile and immobile regions during the
633 migration process controlled by advection–diffusion effect. Due to the low flow
634 velocity characteristics of the immobile region, the process of receiving and releasing
635 solute is very slow, leading to the tailing of the BTC. The MIM model simulates the
636 breakthrough process of solutes in porous media by coupling the solute transfer
637 equations between the mobile and immobile regions within the porous media. For the
638 inert solutes, the governing equations of the MIM model are as followed without
639 considering the adsorption and degradation.

$$\begin{aligned} \theta_m \frac{\partial C_m}{\partial t} + \theta_{im} \frac{\partial C_{im}}{\partial t} &= \theta_m D_m \frac{\partial^2 C_m}{\partial x^2} - v_m \frac{\partial C_m}{\partial x} \\ \frac{\partial C_{im}}{\partial t} &= \alpha(C_m - C_{im}) \end{aligned} \quad (8)$$

$$\beta = \frac{\theta_m}{\theta_{im} + \theta_m} \quad (9)$$

640 where θ_{im} is the total immobile zone ratio, θ_m is the total mobile zone ratio, D is the
641 effective longitudinal dispersion coefficient, v_m is the velocity in mobile region, and α
642 is the first-order mass transfer coefficient (which depends on diffusion coefficient and
643 other geometric factors), C_m and C_{im} represent the concentrations of mobile and
644 immobile regions, respectively, β is the proportion of mobile region in porous media.

645 According to the characteristics of the MIM model, the main flow stream is
646 generalized as the mobile region of the model, and the eddy area is generalized as the

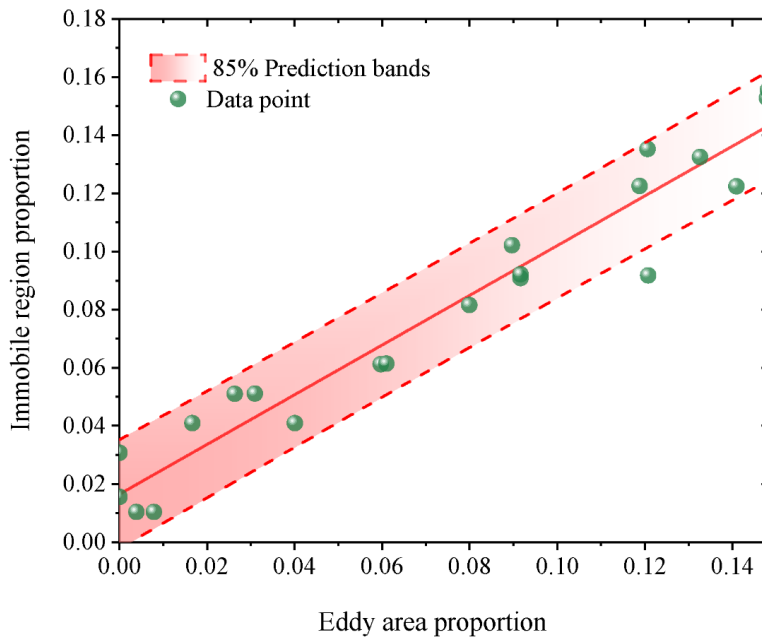


647 immobile region of the model, which show clear physical meaning and provide a basis
648 for parameter inversion of the MIM model. The migration of a pulse solute in porous
649 media can be divided into three different stages: In the initial stage, the concentration
650 of solute in the main flow stream is higher than that in the eddy zone when the solute
651 pulse is first introduced into the porous media, leading to solute migration primarily
652 through advection. During the second stage, as the solute pulse encounters the eddy
653 zone, solute mass transfer occurs due to molecular diffusion, allowing some of the
654 solute mass from the main flow stream to gradually enter the eddies. In the third stage,
655 as the solute pulse moves downstream past the eddy zone, the concentration in the main
656 flow stream decreases rapidly, while the concentration in the eddy zone becomes higher
657 than in the main flow stream. At this point, the solute in the eddy zone diffuses back
658 into the main flow stream, resulting in tailing of the BTCs in the main flow stream.

659 The effect of eddies on solute storage aligns well with the applicable conditions of
660 the MIM model. The eddy zone proportion was obtained directly from the flow field
661 simulations using the quantitative 3D characterization method detailed in Section 3.1,
662 which is based on a critical velocity threshold derived from the velocity PDF/CDF
663 analysis. Conversely, the immobile zone proportion ($1-\beta$) was obtained independently
664 by calibrating the MIM model (Eqs. 8 and 9) against the numerical breakthrough curves
665 (BTCs). To validate whether the eddy proportion is consistent with the immobile region
666 proportion ($1-\beta$) derived from the MIM model, the relationship between the eddy



667 proportion in porous media with varying flow velocities, different particle sizes, and
668 different arrangements was obtained, as shown in Figure 16.



669
670 Figure 16. The relationship between the eddy proportion in porous media with the
671 immobile region proportion ($1-\beta$).

672 The abscissa of Figure 16 represents the eddy area proportion, and the ordinate is
673 the immobile region proportion ($1-\beta$) derived from the MIM model. If the immobile
674 region proportion cluster around the red line with a slope of 1 passing through the origin
675 in the figure, which indicates that generalizing the eddy zone proportion as the
676 immobile region proportion derived from the MIM model is reasonable. We can see
677 from Figure 16 that all data points are located on either side of the red line, with almost
678 all of them falling within the 85% prediction band. The strong correlation observed
679 between these independently obtained parameters validates that the physical eddy zones,



680 identified hydrodynamically, effectively function as the immobile zones in the
681 conceptual MIM model. This provides a physical basis for the MIM parameter and
682 reduces its inversion ambiguity.

683 However, different flow velocities, particle sizes and arrangements will affect the
684 development of eddies in the porous media, influencing the mass transfer process
685 between the main flow stream and the eddy zone. Therefore, we further discussed the
686 variations of the parameters in the MIM model under different control conditions. The
687 mass transfer coefficient (α) and diffusion coefficient (D_{MIM}) are very important
688 parameters in the MIM model, which determines the transfer process between the
689 mobile and immobile region. And the mass transfer coefficient and diffusion coefficient
690 under the influence of different control factors are shown in Table 2.

691 Table 2. The characteristic values of MIM model with different factors.

Average inlet flow velocity (m/s)	Particle size (mm)	D_{MIM}	α	RMSE
0.02		6.00E-04	0.023	0.0027
0.015		5.88E-04	0.009	0.0064
0.01	5	5.41E-04	0.004	0.0043
0.005		4.78E-04	0.001	0.0154
0.002		2.73E-04	0.002	0.0130
0.02		1.73E-03	0.018	0.0060
0.015		1.71E-03	0.012	0.0096
0.01	10	1.57E-03	0.013	0.0150
0.005		1.07E-03	0.010	0.0200
0.002		2.68E-04	0.005	0.0250
Average inlet flow velocity (m/s)	Particle size (mm)	D_{MIM}	α	RMSE

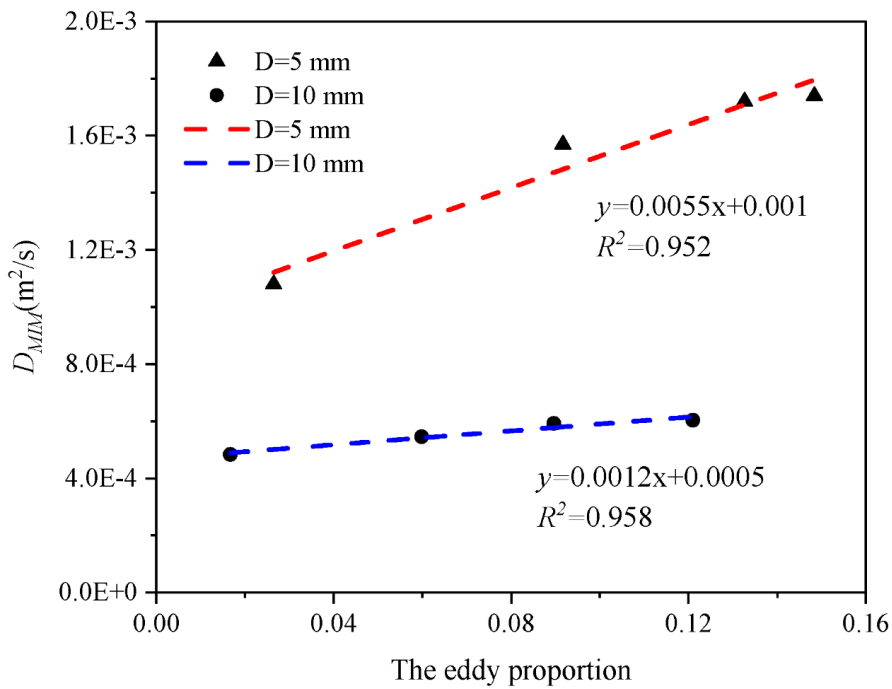


		5	2.27E-05	0.277	0.0077
0.01	8	3.99E-05	0.269	0.0080	
	10	5.98E-05	0.282	0.0064	
	15	1.21E-04	0.303	0.0063	
0.02	5	5.29E-05	0.494	0.0081	
	8	1.04E-04	0.492	0.0074	
	10	1.51E-04	0.490	0.0055	
	15	3.21E-04	0.531	0.0036	
Average inlet flow velocity (m/s)	Arrangement	D_{MIM}	α	RMSE	
0.01	SC	5.98E-05	0.282	0.0064	
	FCC	4.84E-05	0.230	0.0075	
	BCC	3.37E-05	0.096	0.0115	
	RP	4.78E-05	0.110	0.0014	
0.02	SC	1.51E-04	0.490	0.0055	
	FCC	1.05E-04	0.250	0.0026	
	BCC	6.55E-05	0.090	0.0117	
	RP	9.93E-05	0.120	0.0014	

692 The parameters for the Mobile-Immobile Model (MIM) were determined through
693 an inverse modeling procedure directly within the COMSOL Multiphysics®
694 environment. The governing equations of the MIM (Eqs. 8 and 9) were implemented,
695 and the model parameters (including the mass transfer coefficient, the diffusion
696 coefficient in the mobile zone, and the immobile zone ratio) were estimated by coupling
697 the parameter estimation module with a nonlinear least-squares optimization algorithm.
698 This algorithm iteratively adjusted the parameter values to minimize the difference
699 between the simulated breakthrough curves (BTCs) and the concentrations predicted
700 by the MIM, thereby identifying the optimal parameter set that best represents the

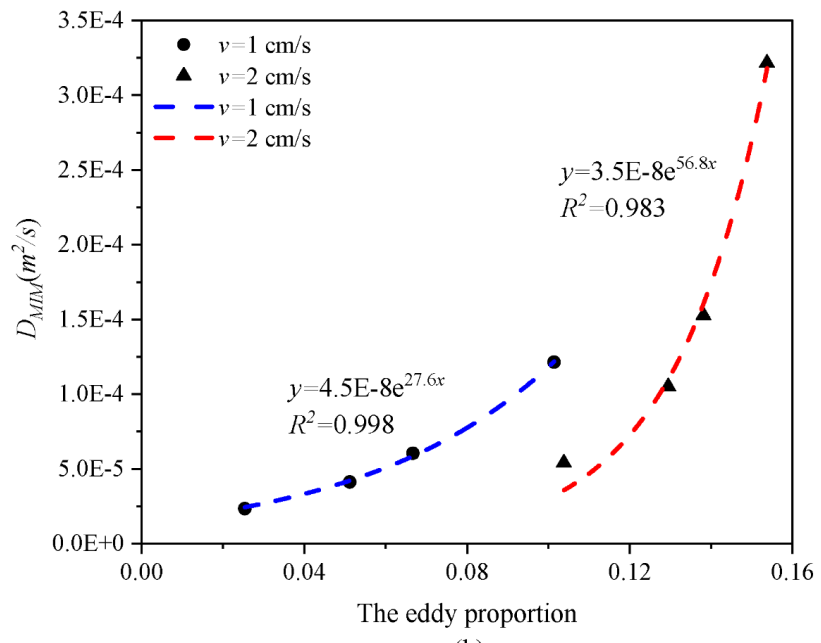


701 observed non-Fickian transport behavior for each specific simulation scenario. To
702 ensure the reliability and uniqueness of the fitted parameters, a sensitivity analysis was
703 conducted, and the root mean square error (RMSE) was calculated for each case, as
704 provided in Table 2. The robustness of the fitted parameters was ensured by verifying
705 the stability of the solution and the convergence of the optimization routine. The mass
706 transfer coefficient and diffusion coefficient increase gradually with the gradual
707 increase of the inlet flow velocity when the particle size remain the same, which is
708 closely related to the development of the eddies. We further obtained the relationship
709 between the eddy proportion corresponding to the three influencing factors and the
710 diffusion coefficient, as shown in Figure 17, and Figures 17(a) and (b) are both SC
711 arrangements.



712

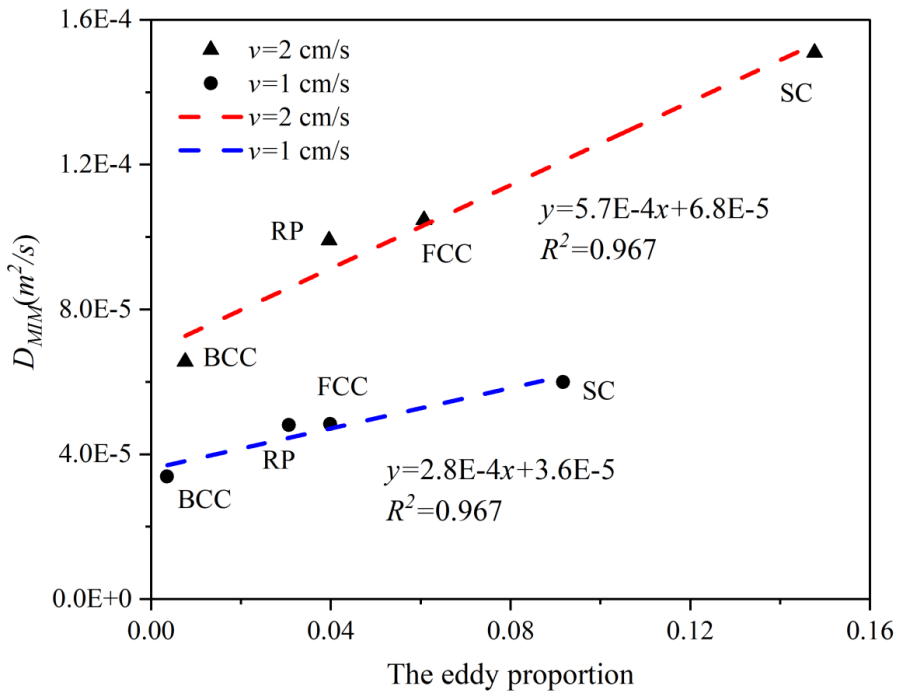
(a)



713

(b)

714



715

716 Figure 17. The relationship between the eddy proportion corresponding to the three
717 influencing factors and the diffusion coefficient.

718 It can be seen from Figure 17(a) that the diffusion coefficient is positively
719 proportional to the eddy proportion. With the increase of inlet flow velocity, on the one
720 hand, the eddy proportion is increased, on the other hand, the rotational velocity of the
721 eddy zone is also increased, then the solute transport process between the main flow
722 stream and the eddy zone and the solute dispersion in the entire porous media are
723 accelerated. In addition, the slope of the red fitting line ($D=10$ mm) in Figure 17 (a) is
724 larger than that of the blue fitting line ($D=5$ mm), which also indicates that the influence
725 of the eddy proportion on the diffusion coefficient is also controlled by different particle
726 sizes. It can be seen from Figure 17(b) that when the inlet flow velocity and arrangement



727 mode (SC) are unchanged, the diffusion coefficient increases exponentially with the
728 eddy proportion. And Figure 17(c) show that the eddy proportion is proportional to the
729 diffusion coefficient under the condition of different arrangement modes, it is found
730 that the larger flow velocity will lead to larger the slope of the linear equation fitted by
731 comparing two different flow velocities.

732 A key insight from this study is the confirmation that eddies act as dynamic regions
733 of active solute retention and release, rather than as immobile water pockets. The
734 measured non-zero velocities within the eddies (Figure 5c) drive a continuous, albeit
735 slower, exchange process with the main flow. This mechanism aligns with the modern
736 understanding of vortex-driven anomalous dispersion, as detailed in studies like
737 [Bordoloi et al. \(2022\)](#). Our findings, which establish a quantitative link between eddy
738 proportion, flow conditions, and the parameters of the MIM model, therefore build upon
739 this paradigm by providing a pore-scale basis for upscaling the effects of such dynamic
740 immobile zones in conceptual and numerical transport models.

741 In addition, the primary objective of this study is to investigate the basic physical
742 mechanisms of eddy-driven non-Fickian transport by isolating key variables in a
743 controlled system. This reductionist approach is a cornerstone of hydrological science,
744 as it allows for the development of fundamental theories and parametric relationships
745 that are often obscured in highly heterogeneous natural systems. The insights gained,
746 specifically, the quantitative links between pore structure, eddy proportion, and the
747 parameters of the Mobile-Immobilized Model (MIM), which provided a mechanistic basis



748 for understanding and predicting solute transport in more complex field scenarios.

749 These include environments where similar processes dominate, such as in coarse-

750 grained aquifer zones, fractured media, or engineered systems like filtration beds. By

751 establishing these fundamental principles, our study provides the scientific basis and

752 conceptual tools needed to improve the accuracy of models used for groundwater

753 pollution prediction and remediation strategy optimization.

754 5 Summary and conclusion

755 The experimental and numerical simulation results of solute transport under three

756 different control factors are presented in this study, and a quantitative characterization

757 method for the eddy proportion on 3D scale is proposed. Besides, the generation,

758 development and evolution of eddies with different factors in different porous media

759 and their effects on solute transport are discussed. The main conclusions are as follows:

760 1. Different types of porous media structures (with varying particle sizes and

761 arrangements) and inlet flow velocities determine the development and evolution of

762 eddies, which in turn affects the solute transport process.

763 2. The exchange of solutes between the main flow stream and the eddy area is slowed

764 down due to the lower flow velocity, resulting in solutes only entering the main flow

765 stream through diffusion, which makes the tailing of the BTCs more pronounced.

766 Smaller particle size will lead to a diminishing trend in the early breakthrough

767 phenomenon of the solute. The penetration process of the BCC model is the fastest,



768 followed by the FCC and SC models, while the penetration process of the RP model is

769 the slowest.

770 3. The proportion of the immobile region inverted by the MIM model can be well
771 matched with that of the eddy zone in porous media. Therefore, taking the eddy area
772 proportion as the input term, on the one hand, endows the parameters of the MIM model
773 with clear physical meanings; On the other hand, taking the structural parameters of
774 porous media as the basis for the inversion of MIM model parameters can optimize the
775 multiple solutions and obtain more accurate model fitting results.

776 4. The mass transfer coefficient (α) and diffusion coefficient (D_{MIM}) of MIM model
777 respond significantly to the different structure of porous media, and the D_{MIM} is
778 proportional to the increase of inlet flow velocity, which is consistent with the results
779 of different arrangement modes. And the D_{MIM} increases exponentially with the eddy
780 proportion when the inlet flow velocity and arrangement mode (SC) are unchanged.

781 **Acknowledgment**

782 This study was supported by the National Natural Science Foundation of China (Grant
783 42407085, 42272296), the Open Fund of Key Laboratory of Mine Ecological Effects
784 and Systematic Restoration, Ministry of Natural Resources (No. MEER-2023-01), and
785 the Natural Science Foundation of Hubei (No. 2025AFB139).

786 **CRediT authorship contribution statement**

787 Zhongxia Li: Writing-review & editing, Writing-original draft, Funding acquisition,
788 Methodology, Conceptualization. Xianshuo Yang: Data curation, Visualization. Shuai



789 Yuan: Writing, Data analysis, Numerical simulation. Junwei Wan: Data curation,
790 Supervision. Yun Yang: Numerical simulation, Data curation. Haibo Feng: Writing-
791 review & editing, Methodology, Visualization. Xixian Kang: Data analysis, Review &
792 Editing. Kun Huang: Numerical simulation, Methodology, Visualization. Chong Ma:
793 Methodology, Data analysis.

794 **Declaration of competing interest**

795 The authors declare that they have no known competing financial interests or personal
796 relationships that could have appeared to influence the work reported in this paper.

797

798

799

800

801

802

803

804

805

806

807

808

809



810 **References**

811 Banaei, S., Javid, A., Hassani, A., 2021. Numerical simulation of groundwater
812 contaminant transport in porous media. *International journal of environmental
813 science and technology*, 18(1): 151-162. DOI:<https://doi.org/10.1007/s13762-020-02825-7>

814

815 Bijeljic, B., Raeini, A., Mostaghimi, P., Blunt, M.J., 2013. Predictions of non-Fickian
816 solute transport in different classes of porous media using direct simulation on
817 pore-scale images. *Physical Review E—Statistical, Nonlinear, Soft Matter
818 Physics*, 87(1): 013011. DOI:<https://doi.org/10.1103/PhysRevE.87.013011>

819

820 Bordoloi, A.D. et al., 2022. Structure induced laminar vortices control anomalous
821 dispersion in porous media. *Nature communications*, 13(1): 3820.
822 DOI:<https://doi.org/10.1038/s41467-022-31552-5>

823

824 Brusseau, M.L., 1994. Transport of reactive contaminants in heterogeneous porous
825 media. *Reviews of Geophysics*, 32(3): 285-313.
826 DOI:<https://doi.org/10.1029/94RG00624>

827

828 Brusseau, M.L., Rao, P., Gillham, R.W., 1989. Sorption nonideality during organic
829 contaminant transport in porous media. *Critical Reviews in Environmental
830 Science Technology*, 19(1): 33-99.
831 DOI:<https://doi.org/10.1080/10643388909388358>

832

833 Burri, N.M., Weatherl, R., Moeck, C., Schirmer, M., 2019. A review of threats to
834 groundwater quality in the anthropocene. *Science of the Total Environment*, 684:
136-154. DOI:<https://doi.org/10.1016/j.scitotenv.2019.05.236>

835

836 Danielopol, D.L., Griebler, C., Gunatilaka, A., Notenboom, J., 2003. Present state and
837 future prospects for groundwater ecosystems. *Environmental conservation*,
30(2): 104-130. DOI:<https://doi.org/10.1017/S0376892903000109>

838

839 de Vries, E.T., Raoof, A., van Genuchten, M.T., 2017. Multiscale modelling of dual-
porosity porous media; a computational pore-scale study for flow and solute
840 transport. *Advances in water resources*, 105: 82-95.
841 DOI:<https://doi.org/10.1016/j.advwatres.2017.04.013>

842

843 Dou, Z., Chen, Z., Zhou, Z., Wang, J., Huang, Y., 2018. Influence of eddies on
844 conservative solute transport through a 2D single self-affine fracture.
845 *International Journal of Heat Mass Transfer*, 121: 597-606.
846 DOI:<https://doi.org/10.1016/j.ijheatmasstransfer.2018.01.037>

847

848 Dou, Z., Sleep, B., Zhan, H., Zhou, Z., Wang, J., 2019. Multiscale roughness influence
849 on conservative solute transport in self-affine fractures. *International Journal of
850 Heat and Mass Transfer*, 133: 606-618.
DOI:<https://doi.org/10.1016/j.ijheatmasstransfer.2018.12.141>

850 Foster, S., Chilton, P.J., 2003. Groundwater: the processes and global significance of
851 aquifer degradation. *Philosophical Transactions of the Royal Society of London.
852 Series B: Biological Sciences*, 358(1440): 1957-1972.
DOI:<https://doi.org/10.1098/rstb.2003.1380>



851 Gao, G. et al., 2010. A new mobile - immobile model for reactive solute transport with
852 scale - dependent dispersion. *Water Resources Research*, 46(8): W08533.
853 DOI:<https://doi.org/10.1029/2009WR008707>

854 Gorelick, S.M., Zheng, C., 2015. Global change and the groundwater management
855 challenge. *Water Resources Research*, 51(5): 3031-3051.
856 DOI:<https://doi.org/10.1002/2014WR016825>

857 Gouze, P., Melean, Y., Le Borgne, T., Dentz, M., Carrera, J., 2008. Non - Fickian
858 dispersion in porous media explained by heterogeneous microscale matrix
859 diffusion. *Water Resources Research*, 44(11): W11416.
860 DOI:<https://doi.org/10.1029/2007WR006690>

861 Grindrod, P., Impey, M.D., 1993. Channeling and Fickian dispersion in fractal
862 simulated porous media. *Water Resources Research*, 29(12): 4077-4089.
863 DOI:<https://doi.org/10.1029/93WR01286>

864 Gruzalski, J.G. et al., 2016. Pore water collection, analysis and evolution: The need for
865 standardization. *Reviews of environmental contamination toxicology* 237: 37-
866 51. DOI:https://doi.org/10.1007/978-3-319-23573-8_2

867 Harr, M.E., 2012. *Groundwater and seepage*. Courier Corporation.
868 DOI:<https://doi.org/10.1126/science.139.3551.205-a>

869 Hasan, S., Joekar - Niasar, V., Karadimitriou, N.K., Sahimi, M., 2019. Saturation
870 dependence of non - fickian transport in porous media. *Water Resources
871 Research*, 55(2): 1153-1166. DOI:<https://doi.org/10.1029/2018WR023554>

872 Hou, Y., Jiang, J., Wu, J., 2018. Anomalous Solute Transport in Cemented Porous
873 Media: Pore - scale Simulations. *Soil Science Society of America Journal*,
874 82(1): 10-19. DOI:<https://doi.org/10.2136/sssaj2017.04.0125>

875 Huang, K. et al., 2013. Experimental investigation on water flow in cubic arrays of
876 spheres. *Journal of Hydrology*, 492: 61-68.
877 DOI:<https://doi.org/10.1016/J.JHYDROL.2013.03.039>

878 Hubbert, M.K., 1940. The theory of ground-water motion. *The Journal of Geology*, 48(8,
879 Part 1): 785-944. DOI:<https://doi.org/10.1086/624930>

880 Jia, Y. et al., 2018. Distribution, formation and human-induced evolution of geogenic
881 contaminated groundwater in China: A review. *Science of the total environment*,
882 643: 967-993. DOI:<https://doi.org/10.1016/j.scitotenv.2018.06.201>

883 Kalhor, K., Ghasemizadeh, R., Rajic, L., Alshawabkeh, A., 2019. Assessment of
884 groundwater quality and remediation in karst aquifers: A review. *Groundwater
885 for sustainable development*, 8: 104-121.
886 DOI:<https://doi.org/10.1016/j.gsd.2018.10.004>

887 Karadimitriou, N.K., Joekar-Niasar, V., Babaei, M., Shore, C.A., 2016. Critical role of
888 the immobile zone in non-Fickian two-phase transport: a new paradigm.
889 *Environmental Science and Technology*, 50(8): 4384-4392.
890 DOI:<https://doi.org/10.1021/acs.est.5b05947>



891 Kaufmann, G., Braun, J., 2000. Karst aquifer evolution in fractured, porous rocks.
892 Water resources research, 36(6): 1381-1391.
893 DOI:<https://doi.org/10.1029/1999WR900356>

894 Kitanidis, P.K., 1994. The concept of the dilution index. Water resources research, 30(7):
895 2011-2026. DOI:<https://doi.org/10.1029/94WR00762>

896 Kohne, J.M., Kohne, S., Mohanty, B.P., Šimunek, J., 2004. Inverse mobile-immobile
897 modeling of transport during transient flow: Effects of between-domain transfer
898 and initial water content. Vadose Zone Journal, 3(4): 1309-1321.
899 DOI:<https://doi.org/10.2113/3.4.1309>

900 Koohbor, B. et al., 2023. The effects of water table fluctuation on LNAPL deposit in
901 highly permeable porous media: A coupled numerical and experimental study.
902 Journal of Contaminant Hydrology, 256: 104183.
903 DOI:<https://doi.org/10.1016/j.jconhyd.2023.104183>

904 Kreft, A., Zuber, A., 1978. On the physical meaning of the dispersion equation and its
905 solutions for different initial and boundary conditions. Chemical Engineering
906 Science, 33(11): 1471-1480. DOI:[https://doi.org/10.1016/0009-2509\(78\)85196-3](https://doi.org/10.1016/0009-2509(78)85196-3)

907 Lee, J., Babadagli, T., 2021. Effect of roughness on fluid flow and solute transport in a
908 single fracture: A review of recent developments, current trends, and future
909 research. Journal of Natural Gas Science Engineering, 91: 103971.
910 DOI:<https://doi.org/10.1016/j.jngse.2021.103971>

911 Li, Y., Chen, L., Shi, Y., 2023. Influence of 3D Fracture Geometry on Water Flow and
912 Solute Transport in Dual-Conduit Fracture. Water, 15(9): 1754.
913 DOI:<https://doi.org/10.3390/w15091754>

914 Li, Z. et al., 2024. On the advection-diffusion process with developing eddies in karst
915 conduits. Geophysical Research Letters, 51(23): e2024GL111214.
916 DOI:<https://doi.org/10.1029/2024GL111214>

917 Llamas, M.R., Martínez-Santos, P., 2005. Intensive groundwater use: silent revolution
918 and potential source of social conflicts. Journal of water resources planning
919 management, 131(5): 337-341. DOI:[https://doi.org/10.1061/\(ASCE\)0733-9496\(2005\)131:5\(337\)](https://doi.org/10.1061/(ASCE)0733-9496(2005)131:5(337))

920 Moradi, G., Mehdinejadiani, B., 2018. Modelling Solute Transport in Homogeneous
921 and Heterogeneous Porous Media Using Spatial Fractional Advection-
922 Dispersion Equation. Soil Water Research, 13(1): 18-28.
923 DOI:<https://doi.org/10.17221/245/2016-SWR>

924 Polubarnova-Kochina, P.Y., 2015. Theory of ground water movement. Princeton
925 university press. DOI:<http://www.jstor.org/stable/j.ctt183pgm>.

926 Rao, P., Rolston, D., Jessup, R., Davidson, J., 1980. Solute transport in aggregated
927 porous media: Theoretical and experimental evaluation. Soil Science Society of
928 America Journal, 44(6): 1139-1146.
929 DOI:<https://doi.org/10.2136/sssaj1980.03615995004400060003x>



932 Šimunek, J., He, C., Pang, L., Bradford, S., 2006. Colloid-facilitated solute transport
933 in variably saturated porous media: Numerical model and experimental
934 verification. *Vadose zone journal*, 5(3): 1035-1047.
935 DOI:<https://doi.org/10.2136/vzj2005.0151>

936 Shah, T., Roy, A.D., Qureshi, A.S., Wang, J., 2003. Sustaining Asia's groundwater
937 boom: an overview of issues and evidence, *Natural Resources Forum*. Wiley
938 Online Library, pp. 130-141. DOI:<https://doi.org/10.1111/1477-8947.00048>

939 Tang, D., Frind, E., Sudicky, E.A., 1981. Contaminant transport in fractured porous
940 media: Analytical solution for a single fracture. *Water resources research*, 17(3):
941 555-564. DOI:<https://doi.org/10.1029/WR017i003p0055>

942 Vaughan, P., 2009. Assumption, prediction and reality in geotechnical engineering,
943 Selected papers on geotechnical engineering by PR Vaughan. Thomas Telford
944 Publishing, pp. 305-341. DOI:<https://doi.org/10.1680/geot.1994.44.4.573>

945 Wang, Y., Zheng, C., Ma, R., 2018. Safe and sustainable groundwater supply in China.
946 *Hydrogeology Journal*(5): 1301-1324. DOI:<https://doi.org/10.1007/s10040-018-1795-1>

947 Wang, Z., 2004. Seepage in Soils—Principles and Applications. *Vadose Zone Journal*,
948 3(2): 728-729. DOI:<https://doi.org/10.2136/vzj2004.0728>

949 Xiong, T. et al., 2024. Two-dimensional high-resolution numerical investigation of
950 eddy effect in artificial rough conduits with different shapes. *Advances in Water
951 Resources*, 184: 104621. DOI:<https://doi.org/10.1016/j.advwatres.2024.104621>

952 Yang, X., Ji, Z., Zhang, P., Qi, J., 2019. Model test and numerical simulation on the
953 development of artificially freezing wall in sandy layers considering water
954 seepage. *Transportation Geotechnics*, 21: 100293.
955 DOI:<https://doi.org/10.1016/j.trgeo.2019.100293>

956 Yu, P. et al., 2023. A pore-scale numerical study on the seepage characteristics in low-
957 permeable porous media. *Environmental Earth Sciences*, 82(11): 268.
958 DOI:<https://doi.org/10.1007/s12665-023-10953-9>

959 Zheng, L., Wang, L., Wang, T., Wang, Z.-L., Chen, X., 2022. Mass transfer between
960 recirculation zone and main flow domain in fractures: Is the first order rate law
961 valid? *Journal of Hydrology*, 613: 128352.
962 DOI:<https://doi.org/10.1016/j.jhydrol.2022.128352>

963 Zhou, J.-Q., Li, C., Wang, L., Tang, H., Zhang, M.J.J.o.H., 2021. Effect of slippery
964 boundary on solute transport in rough-walled rock fractures under different flow
965 regimes. *Journal of Hydrology*, 598: 126456.
966 DOI:<https://doi.org/10.1016/j.jhydrol.2021.126456>

967 Zhou, J.Q., Wang, L., Chen, Y.F., Cardenas, M.B., 2019. Mass transfer between
968 recirculation and main flow zones: Is physically based parameterization
969 possible? *Water Resources Research*, 55(1): 345-362.
970 DOI:<https://doi.org/10.1029/2018WR023124>

971



972 Zhou, L., Selim, H., 2003. Application of the fractional advection - dispersion equation
973 in porous media. Soil Science Society of America Journal, 67(4): 1079-1084.
974 DOI:<https://doi.org/10.2136/sssaj2003.1079>

975